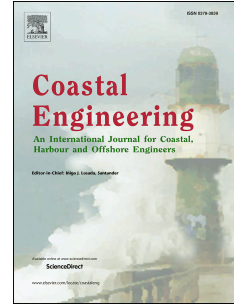


Journal Pre-proof

Modelling wave attenuation by quasi-flexible coastal vegetation

Thomas J. van Veelen, Harshinie Karunaratna, Dominic E. Reeve



PII: S0378-3839(20)30506-8

DOI: <https://doi.org/10.1016/j.coastaleng.2020.103820>

Reference: CENG 103820

To appear in: *Coastal Engineering*

Received Date: 25 September 2019

Revised Date: 9 November 2020

Accepted Date: 21 November 2020

Please cite this article as: van Veelen, T.J., Karunaratna, H., Reeve, D.E., Modelling wave attenuation by quasi-flexible coastal vegetation, *Coastal Engineering*, <https://doi.org/10.1016/j.coastaleng.2020.103820>.

This is a PDF file of an article that has undergone enhancements after acceptance, such as the addition of a cover page and metadata, and formatting for readability, but it is not yet the definitive version of record. This version will undergo additional copyediting, typesetting and review before it is published in its final form, but we are providing this version to give early visibility of the article. Please note that, during the production process, errors may be discovered which could affect the content, and all legal disclaimers that apply to the journal pertain.

© 2020 The Author(s). Published by Elsevier B.V.

Thomas J. van Veelen: Conceptualization, Methodology, Investigation, Validation, Formal analysis, Writing – Original Draft. **Harshinie Karunarathna:** Conceptualization, Methodology, Writing – Review & Editing, Supervision. **Dominic E. Reeve:** Resources, Writing – Review & Editing, Supervision.

Journal Pre-proof

1 Modelling wave attenuation by quasi-flexible coastal vegetation

2
3 Thomas J. van Veelen^{1*}, Harshinie Karunaratna^{1**}, Dominic E. Reeve^{1***}

4
5 ¹ Energy and Environment Research Group, Zienkiewicz Centre for Computational Engineering,
6 Swansea University, SA1 8EN, Swansea, United Kingdom

7 * Corresponding author: thomas.vanveelen@swansea.ac.uk

8 ** H.U.Karunaratna@Swansea.ac.uk

9 *** D.E.Reeve@Swansea.ac.uk

10 11 Abstract

12 Coastal vegetation such as seagrasses, salt marshes, and mangroves, contributes to coastal defence
13 by damping incoming waves. Yet, plant species differ in flexibility due to which they interact
14 differently with incoming waves and damp waves to a variable degree. Current wave damping
15 models struggle to balance accuracy against computational costs when accounting for wave-
16 vegetation interaction. Instead, they often rely on a plant-specific calibration of the drag coefficient,
17 which limits their application across plant species. Here we show, using novel simultaneous
18 experimental data of wave damping, water velocities and stem motion, that wave damping by quasi-
19 flexible cylindrical vegetation is controlled by the relative velocity between water and vegetation at
20 the upright bottom section of a stem. For the quasi-flexible vegetation conditions considered in this
21 manuscript ($L > 1.4$ and $Ca < 700$), our experimental evidence justifies the application of a model
22 based on the Euler-Bernoulli beam theory to estimate plant motion when the stem length is smaller
23 than the wave excursion. Building on the solution of plant motion, we simulate wave damping over
24 flexible vegetation fields through a new work factor. Our model successfully predicts damping of
25 regular waves by rigid and flexible artificial vegetation, and real *S. Anglica*, *P. Maritima* and *E.*
26 *Athericus* plants in the right order of magnitude under medium and high energy wave conditions.
27 The simulated wave damping is directly linked to vegetation and wave conditions and does not
28 require plant-specific calibration of the drag coefficient. It is anticipated that the model will be of
29 wide practical use in simulating wave damping by quasi-flexible cylindrical coastal vegetation across
30 large areas with diverse plant species and wave conditions.

31
32 **Keywords:** Flexible vegetation, Nature-based coastal defences, Vegetation modelling, Wave
33 damping, Salt marshes.

34
35 **Declarations of interest:** none.

36 37 1. Introduction

38
39 Coastal vegetation is found around the globe in the form of seagrass fields, kelp forests, salt marshes
40 and mangrove forests [36]. The vegetation between and within these habitats differs significantly,
41 ranging from flexible grasses to rigid shrubs and trees. When vegetation is present on or seaward of
42 the coastline, it interacts with incoming waves [23].

43
44 Vegetation contributes to coastal protection by damping incoming waves [16,24,34]. When waves
45 travel over vegetation, energy is dissipated due to the work done by wave forces on plants [10]. This
46 can significantly reduce wave impact on beaches and hard structures, lowering their construction
47 and maintenance costs [46,48]. Additionally, vegetation reduces storm surge propagation and
48 stabilises shorelines during storms, and contributes to sediment capture, carbon storage and
49 recreational opportunities outside storm events [5,12,43,45,49].

50

51 Stem motion of flexible vegetation can impact wave damping significantly as has been demonstrated
52 in experimental [27,38,40] and numerical studies [29,35]. Vegetation species are broadly classified
53 as rigid or flexible. Rigid vegetation, like woody shrubs, does not move over a wave cycle, whereas
54 flexible vegetation, like thin grass, sways as its rigidity is insufficient to resist stem bending. The
55 excursion of flexible species increases when its flexural rigidity decreases or wave forces increase
56 [27]. As stem bending increases, the plant frontal area and the relative velocity between water and
57 stem decrease [33,38]. Both limit the wave forces on the plant and may reduce wave damping by up
58 to 50-70% [27,35,40,47]. However, as the interaction between plant motion and wave forces is
59 reciprocal, quantifying wave damping over flexible species poses a challenge.

60
61 Numerical models can be a valuable tool to quantify wave damping for variable vegetation
62 properties. For rigid vegetation, Dalrymple et al. [10] simplified vegetation fields to arrays of rigid
63 cylinders on a flat bottom and assumed validity of linear wave theory to model damping of
64 monochromatic waves. Under these assumptions, they demonstrated that wave damping is
65 dominated by drag, and wave heights reduce proportionally to the distance travelled over
66 vegetation. Using the same modelling framework, Mendez & Losada [32] proposed to calibrate the
67 drag coefficient to include the effect of stem motion. Their model was successfully applied in field
68 [6,13,16] and flume studies [2,3,18,24,34,47], but the calibrated drag coefficients vary widely
69 between plant species and test conditions [36,48], and when vegetation conditions change [42].
70 Thus, site-specific calibration for each coastal habitat is required.

71
72 Alternatively, an effective stem length can be employed to include the effect of stem bending in a
73 rigid vegetation model. The effective stem length is the height of a rigid stem that generates equal
74 drag as that of the (longer) flexible stem [28]. Paul et al. [38] proposed using observed frontal area
75 as the effective vegetation length, based on experiments with lexan strips. Instead, Luhar et al. [27]
76 fitted an analytical model for the effective length of flexible seagrass based on a scaling analysis of
77 the equations of stem motion but suggested that different fits for different species are required.
78 Their model was expanded to a predictive model for wave damping by Lei and Nepf [22], who
79 further discriminated between rigid and flexible stem sections and introduced a new fit for the
80 effective stem length.

81
82 Other models have included vegetation motion explicitly by modelling stems as flexible rods.
83 Mendez et al. [33] solved the excursion of the tip using stem-averaged velocities and a linearised
84 drag force in an idealised model. Vertical variations in the velocity profile were included by
85 Mullarney & Henderson [35] and the buoyancy force was included in Henderson [14]. However,
86 these models are limited to stems with small deflections. Alternatively, complex numerical models
87 included friction, inertia and buoyancy forces to solve stem motion under strong plant bending for
88 individual stems [21,29] and vegetation fields [9,30]. However, the computational cost for these
89 models is high, which makes them unsuitable for large areas.

90
91 The various modelling approaches show a trade-off between complexity, accuracy, computational
92 cost, and applicability, but the optimal balance for practical cases remains unclear. Simple models
93 can be easily applied, but require site and plant-specific calibration. Alternatively, complex models
94 add processes which can reduce the variation in calibration, but at a computational cost and
95 potentially increasing model errors. Therefore, the accuracy gains by including additional
96 mechanisms must be carefully weighed against the extra computational costs. Furthermore, no
97 complex model has been successfully validated across multiple species of real vegetation that differ
98 in flexibility.

99
100 In the present study, we aim to provide a novel versatile mathematical modelling framework for
101 wave damping over coastal vegetation under quasi-flexible vegetation conditions. Quasi-flexible

102 vegetation conditions are defined as flexible vegetation that does not fold over or fully extent during
 103 a wave cycle. A balance between complexity and applicability is obtained by including only the key
 104 mechanisms involved in the wave-vegetation interaction. These mechanisms are identified by, for
 105 the first time, combining experimental data of wave damping, wave velocity fields, and plant
 106 motion. Based on the key physics, we develop a new modelling framework with applicability across
 107 cylindrical vegetation species and hydrodynamic conditions without the need for plant-specific
 108 calibration.

109

110 This manuscript is structured as follows: Section 2 discusses the wave-vegetation interaction.
 111 Section 3 presents and discusses the novel experimental data with the aim of justifying model
 112 assumptions. The modelling framework is described in Section 4 and validated in Section 5. Finally,
 113 conclusions are provided in Section 6.

114

115 2. Theoretical background

116

117 2.1 Coordinate system

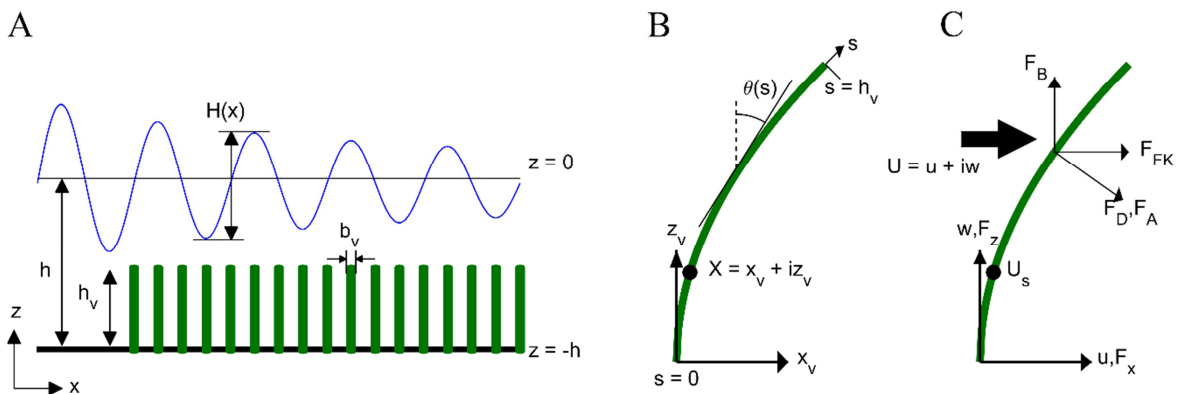
118

119 Let us define a coordinate system at canopy-scale (Fig. 1a), where waves travel over a vegetation
 120 field on top of a flat bed. The direction of wave propagation is normal to the canopy and parallel to
 121 the x -axis with $x = 0$ at the upstream edge of the vegetation. The z -axis describes vertical position
 122 with respect to the water column such that $z = 0$ depicts the still water surface and $z = -h$ the bed
 123 level. The waves are modelled by their height $H(x)$, period T and velocity field $U(x, z, t) = u + iw$,
 124 where the real and complex parts denote the horizontal and vertical directions respectively.

125

126 A single stem in the canopy is modelled as a cylinder with height h_v , diameter b_v , and flexural
 127 rigidity EI_v . Cylinders are an accepted geometry for coastal vegetation types such as salt marsh
 128 grasses [16,41], mangrove branches [44] and coral [25]. Stem density n_v defines the number of
 129 stems per unit ground area. We introduce a plant-scale coordinate system to define stem motion
 130 (Fig. 1b). Along-stem coordinate s is defined such that $s = 0$ is the root and $s = h_v$ is the tip of the
 131 stem. Stem posture $X(s, t) = x_v + iz_v$ follows the complex coordinate system. The stem moves at
 132 velocity $U_{veg} = \partial X / \partial t$ and its bending with respect to an upright stem is defined by bending angle
 133 $\theta(s, t)$. Finally, we define wave velocities $U_s(s, t) = u_s + iw_s$ and forces $F(s, t) = F_x + iF_z$ at the
 134 stem (Fig. 1c).

135



136

137 *Figure 1: Definition sketches of the coordinate system of the wave-vegetation interface at the (A) canopy and (B) plant*
 138 *scales. (C) shows the velocities and forces at the plant scale.*

139 Dimensionless parameters will be employed for all variables throughout this manuscript (denoted by
 140 asterisks). We introduce scaled coordinates

141

$$x_* = \frac{x}{A_w}, \quad z_* = \frac{z}{h_v}, \quad s_* = \frac{s}{h_v}, \quad t_* = t\omega, \quad (1)$$

142

143 and quantities

144

$$X_* = \frac{X}{h_v}, \quad H_* = \frac{H}{h}, \quad U_* = \frac{U}{u_c}, \quad U_{veg*} = \frac{U_{veg}}{u_c}, \quad F_* = \frac{F}{\rho b_v u_c^2}. \quad (2)$$

145

146 Herein, $\omega = 2\pi/T$ is the wave angular frequency, u_c is the velocity scale, $A_w = u_c/\omega$ is the typical
 147 wave excursion length, and $\rho = 1000 \text{ kg/m}^3$ is the water density. u_c is defined as amplitude of the
 148 horizontal wave orbital motion [15] according to

149

$$u_c = \frac{1}{2}(u_f + u_b) \quad (3)$$

150

151 where u_f is the peak forward velocity, u_b is the peak backward velocity, and $\nu = 10^{-6} \text{ m}^2/\text{s}$ is the
 152 kinematic viscosity of water. u_f and u_b may be measured or based on linear wave theory. Hu et al.
 153 [15] measured velocities halfway of the water column, which was between 1/3 and 2/3 of the
 154 vegetation height. However, it is more appropriate to define the velocity scale relative to the
 155 vegetation height, rather than the water column, for moving vegetation. Therefore, we consider the
 156 velocities halfway the vegetation height, which is the average of the height range used in Hu et al.
 157 [15]. Furthermore, we introduce two dimensionless quantities that control wave-vegetation
 158 interaction for flexible vegetation [27]: the Cauchy number

159

$$Ca = \frac{\rho b_v u_c^2 h_v^3}{EI_v} \quad (4)$$

160

161 being the ratio between wave forces and stem stiffness, and the excursion ratio

162

$$L = \frac{h_v}{A_w} \quad (5)$$

163

164 being the ratio between stem length and wave excursion.

165

166 2.2 Wave-vegetation interaction

167

168 Vegetation interacts with dynamic forces induced by waves and the static buoyancy force (Fig. 1c).
 169 The interaction is one-way for rigid vegetation and two-way for flexible vegetation. We consider
 170 three wave-induced forces that act on vegetation. These are given per unit stem length: the drag
 171 force;

172

$$F_{D_*} = \frac{1}{2} C_D |u_{rn*}| u_{rn*} e^{-i\theta}, \quad (6)$$

173

174 the added mass force;

175

$$F_{A_*} = \frac{1}{2} C_A \frac{\pi^2}{KC} \frac{\partial u_{rn*}}{\partial t_*} e^{-i\theta}, \quad (7)$$

176

177 the Froude-Krylov force;

178

$$F_{FK*} = \frac{1}{2} \frac{\pi^2}{KC} \frac{\partial U_{S*}}{\partial t_*}. \quad (8)$$

179

180 Herein, $u_{rm*} = \Re(U_{r*}e^{i\theta})$ and $u_{rp*} = \Im(U_{r*}e^{i\theta})$ are the stem-normal and stem-parallel
 181 components of the relative velocity between water and stem $U_{r*} = U_{S*} - U_{veg*}$. C_D and C_A are
 182 coefficients for drag and added mass respectively and $KC = u_c T / b_v$ is the Keulegan-Carpenter
 183 number. The drag coefficient

184

$$C_D = \left(\frac{730}{Re}\right)^{1.37} + 1.04 \quad (9)$$

185

186 was derived via direct force measurements on field of rigid cylinders in the range $300 < Re < 4700$
 187 by Hu et al. [15], where $Re = u_c b_v / \nu$ is the vegetation Reynolds number. Although KC may also be
 188 a strong predictor for C_D [8,17,37], Re has been selected in this study as Eq. 9 was derived via direct
 189 force measurements. The drag coefficient is commonly calibrated to include the effect of vegetation
 190 swaying [e.g. 32] but in this study we include plant motion explicitly such that Eq. 9 is applied to all
 191 vegetation types in this study. $C_A = 12.63KC^{0.0583} - 15.09$ satisfies empirical data by Keulegan &
 192 Carpenter [17] for $KC \geq 20$. We note that their C_M equals $C_A + 1$ in this study as we define the
 193 added mass and Froude-Krylov forces separately [11]. The friction force, based on Zeller et al. [50], is
 194 of negligible magnitude for the conditions considered here ($Re = 570-1500$) and therefore omitted.

195

196 The magnitude of F_{A*} and F_{FK*} relative to F_{D*} is controlled by the ratio $\pi^2 / (KC|u_{rm*}|)$. KC is of the
 197 order $O(10^2)$ for conditions considered in this study as is realistic for field conditions [16]. In case of
 198 rigid vegetation, $|u_{rm*}| = |u_{S*}| = O(10^0)$ and the relative magnitude of F_{A*} and F_{FK*} is of order
 199 $O(10^{-1})$. The same scaling argument has also been employed for flexible vegetation [e.g. 35], but
 200 when the relative velocity reduces due to vegetation swaying, F_{A*} and F_{FK*} may be of similar
 201 magnitude as F_{D*} . Therefore, we do consider F_{A*} and F_{FK*} at this stage of our analysis. Finally, the
 202 net buoyant force

203

$$F_{B*} = \frac{1}{4} \pi (\rho' - 1) \frac{g b_v}{u_c^2} i \quad (10)$$

204

205 is not exerted by waves but can modify plant posture [50]. It features $g = 9.81 \text{ m/s}^2$ as the
 206 gravitational acceleration and $\rho' = \rho_v / \rho$ as the ratio between the vegetation density (ρ_v) and the
 207 water density.

208

209 Swaying by flexible vegetation affects the magnitude and direction of the wave forces (Eq. 6-8). We
 210 consider inextensible stems, homogeneous cylindrical cross-sections, homogeneous flexural rigidity,
 211 and no interaction between stems. Instead, the sheltering of downstream vegetation can be
 212 included through the velocity scale (Eq. 3). Under these conditions, plant motion is controlled by the
 213 force balance [29,35], according to

214

$$\frac{1}{2} \frac{\pi^2}{KC} \rho' Ca \frac{\partial U_{veg*}}{\partial t_*} + \left(\frac{\partial^3 \theta}{\partial s_*^3} - i \frac{\partial \theta}{\partial s_*} \frac{\partial^2 \theta}{\partial s_*^2} \right) e^{-i\theta} = Ca (F_{D*} + F_{A*} + F_{FK*} + F_{B*}). \quad (11)$$

215

216 The first term on the left-hand side is the stem inertia and the second term expresses bending
 217 resistance. The wave and buoyancy forces control plant motion via the forcing term on the right-
 218 hand side. Conversely, plant motion controls the direction and the magnitude of the wave forces.
 219 This two-way interaction between wave forces and stem motion poses the main challenge in solving
 220 wave forces on flexible vegetation. Therefore, our experiments, described in Section 3, aim to
 221 identify the key physical interactions relevant to wave damping to justify simplifications of Eq. 11.

222 Specifically, we will investigate the relative magnitude of F_{A*} and F_{FK*} , the predominant stem
 223 section that contributes to stem bending, and whether the effect of plant bending on force direction
 224 (stem reconfiguration) or relative velocity (stem velocity) is most important.

225 226 **2.3 Wave damping**

227
228 Dalrymple et al. [10] showed that wave damping over a flat bottom is controlled by the conservation
 229 of wave power, which is given in its dimensionless form by

$$230 \quad c_{g*} \frac{\partial E_*}{\partial x_*} = -8\lambda_f F_r^2 D^{-1} \epsilon_{v*} \quad (12)$$

231
232 where $E_* = H_*^2$ is the wave energy and $c_{g*} = \frac{1}{2k_*} + \frac{D}{\sinh 2k_* D}$ is the wave group velocity. We have
 233 introduced $\lambda_f = n_v b_v h_v$ as the frontal area per unit ground area [7,25], $F_r = u_c / \sqrt{gh}$ as the Froude
 234 number, $D = h/A_w$ as the ratio between water depth and wave excursion, and $k_* = kA_w$ as the
 235 dimensionless wave number. Furthermore, ϵ_{v*} is the energy dissipation per stem due to the work
 236 done by wave forces given by

$$237 \quad \epsilon_{v*} = \int_{s_*=0}^1 \overline{F_{D*} \cdot U_{S*}} ds_* \quad (13)$$

238
239 Here the overbar denotes phase-averaging over a wave cycle. Although F_{A*} and F_{FK*} can be of
 240 sufficient magnitude to control plant motion, they act out of phase with the water motion such that
 241 their phase-averaged work done is considered to be negligible. This argument strictly requires that
 242 the phase difference between U_{S*} and u_{rn*} is small, which is reasonable given that the phase
 243 difference between water and stem motion reduces when vegetation velocities increase [35].
 244 Finally, we will employ

$$245 \quad W_* = F_* \cdot U_{S*} \quad (14)$$

246
247 as a short-hand notation for the time-dependent work done (W_*) by waves per unit stem length.

248
249 The solution of Eq. 12 in terms of wave height expresses a decay in the direction of wave
 250 propagation. In case of rigid vegetation, Dalrymple et al. (1984) showed that the solution in terms of
 251 wave damping is given by

$$252 \quad H_* = \frac{H_{0*}}{1 + \beta_* x_*} \quad (15)$$

253
254 Where H_{0*} is the incident wave height and β_* is the damping coefficient, scaled as $\beta_* = \beta A_w$. In case
 255 of flexible vegetation, Eq. 15 holds when the vegetation dynamics remain constant, i.e. u_{rn*} damps
 256 proportionally to H_* . This is assumed to be the case in this study given that the vegetation fields in
 257 our experiments and validation cases are short with a length of 1.5 m and up to 40 m respectively.

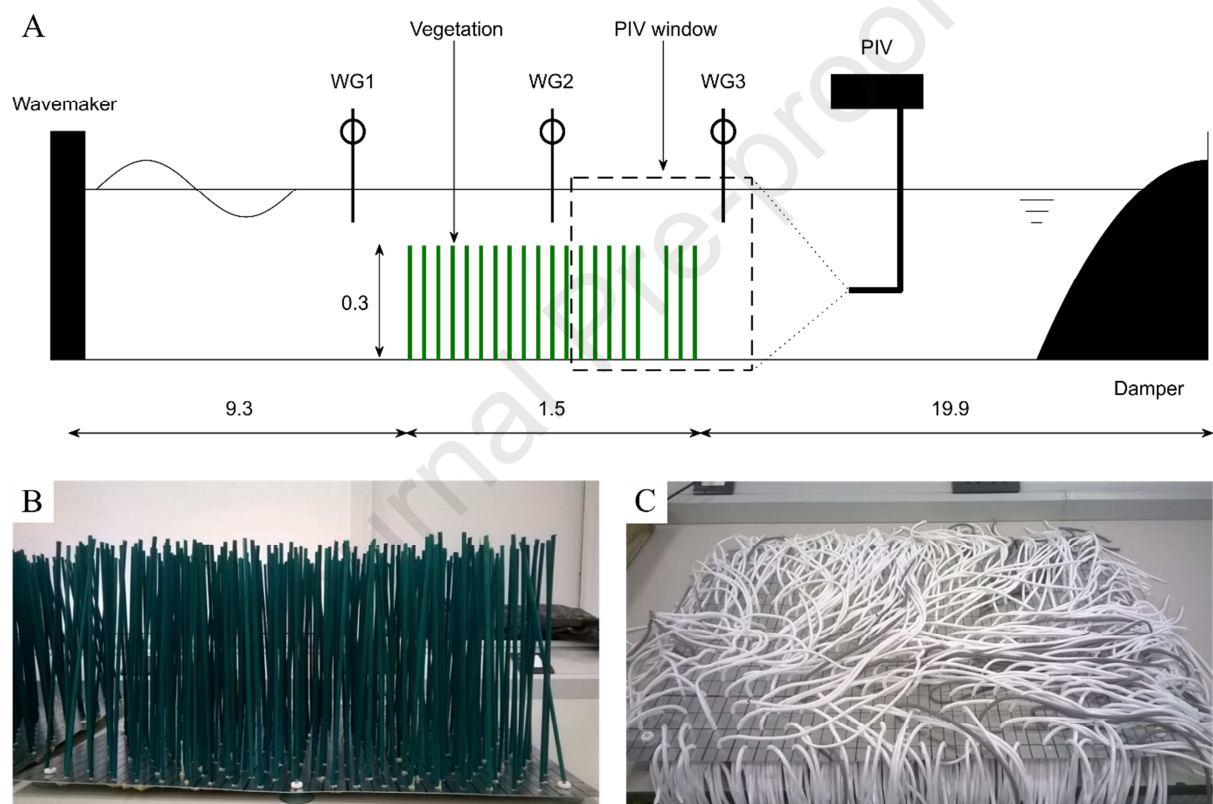
258 259 **3. Wave damping analysis under observed plant motion**

260 261 **3.1 Laboratory experimental setup**

262
263 Experiments of wave damping over rigid and flexible vegetation canopies were conducted in the
 264 wave flume of the Coastal Laboratory of Swansea University, UK, to identify key mechanisms in the

265 wave-vegetation interaction. The wave flume measures 30.7m in length, 0.8m in width and 1.2m in
 266 height. It has a piston-type wavemaker with active wave absorption at one end and a parabolic wave
 267 damper of reticulated foam at the other end (Fig. 2a). We measured wave height, the water particle
 268 velocity field and plant motion simultaneously. By observing plant motion, we avoid solving the force
 269 balance (Eq. 11) as a requirement to calculate wave-induced forces (Eq. 6-8).

270
 271 Cylindrical rigid and flexible mimic canopies were fixed on the floor of the wave flume. The two
 272 stem types differed only in flexural rigidity. Rigid vegetation was created from bamboo dowels with
 273 $EI_v = 9.0 \pm 4 \times 10^{-2} \text{ Nm}^2$ (mean \pm standard deviation, measured using three-point bending
 274 testing). Silicon sealants were used to construct flexible vegetation with $EI_v = 1.7 \pm 0.3 \times 10^{-5}$
 275 Nm^2 . All stems were 300 mm in height and had a diameter of 5 mm. Stems were aligned in a
 276 staggered formation to form a canopy with a length of 1.5 m and a stem density of 1111 stems/ m^2 . A
 277 90mm wide section was cleared near the downstream edge of the canopy for velocity
 278 measurements at 1.35m from the upstream edge of the vegetation field.
 279



280
 281 *Figure 2: (A) Sketch of the experimental set-up. All dimensions are in metres. Figure is not to scale; (B) Artificial rigid*
 282 *vegetation; (C) Artificial flexible vegetation.*

283 The vegetation patches were subjected to regular waves with variation in height, period, and water
 284 depth. The wave height varied between 0.08 and 0.20 m, the wave period between 1.4 and 2.0 s,
 285 and water depth between 0.30 and 0.60 m. The 24 test conditions (Table 1) were selected to
 286 represent a range of wave intensities. Each condition was run three times as reflection limited the
 287 number of undisturbed waves per run to 3-12 (Fig. 3a, left), which included a control run with
 288 reversed vegetation field to verify that the gap in the canopy did not affect wave dynamics. Although
 289 wave input was monochromatic, second order Stokes waves were observed due to shallow water
 290 conditions [20]. Videos of the wave-vegetation interaction under conditions R3, R13, R23 and R33
 291 can be found in the supplementary materials.

292
 293 Wave heights were measured using three resistance type wave gauges (HR Wallingford, accuracy
 294 ± 0.1 mm). They were located upstream (WG1, 8.2 m downstream of the wave paddle), halfway

295 (WG2, 10.0 m) and downstream (WG3, 10.8 m) of the vegetation patches. Wave measurements
 296 started when the water level had reached 95% of the incident wave amplitude and at least five
 297 waves had passed, and were terminated when the first reflected wave would reach the vegetation
 298 field based on shallow water wave theory. A single damping coefficient β_{exp} was fitted to Eq. 15 via
 299 the least-squares method using combined data of all three runs, providing 5 degrees of freedom (Fig.
 300 3a, right). The damping coefficients of each condition and their confidence intervals are provided in
 301 Table 1. The average width of the 95% confidence interval (CI) of β_{exp} was 0.013 m^{-1} for rigid
 302 vegetation and 0.012 m^{-1} for flexible vegetation. The observed wave damping was significant with at
 303 least 3.3 mm, far exceeding the measurement error (0.1 mm). Furthermore, β_{exp} exceeded the
 304 width of the 95% CI for all but one test case (R4, flexible). It was verified through control runs that
 305 the damping over the flume floor was negligible ($\beta < 0.005$).

306
 307 Water particle velocity fields inside and around vegetation were measured using Particle Image
 308 Velocimetry (PIV; Dantec systems). Polyamide seeding particles that follow water motion were
 309 added to the wave flume. These were tracked by a high-speed camera under laser illumination. The
 310 raw velocity field time series was obtained by cross-correlation of particle positions over consecutive
 311 camera frames. Following Luhar & Nepf [29], a Fourier filter was applied to remove noise from the
 312 raw velocity time series. We retained only the wave-averaged velocities, the natural harmonic and
 313 the first higher order harmonic (Fig. 3b). The velocity time series aligned closely to the wave time
 314 series but were restricted to 11s due to the limitations on the number of frames that can be
 315 captured by the PIV-camera each run.

316
 317 The velocity at rigid stems was derived from the water particle velocities inside the canopy. The
 318 velocity structure was considered fully developed as the gap was more than five drag length scales
 319 [25] downstream of the canopy edge. The control runs with reversed vegetation prevented velocity
 320 measurements for one run per condition. Alternatively, the velocity at flexible stems was derived
 321 from the vertical velocity structure at the downstream edge for which stem motion can be identified
 322 simultaneously. Based on comparisons with control runs without vegetation, we found that flexible
 323 vegetation did not disturb the flow velocity structure apart from damping proportional to the wave
 324 height. Hence, the wave-vegetation interaction at the downstream edge is assumed to be
 325 representative for the whole canopy when velocity damping is accounted for.

326
 327 Wave-averaged currents were observed within rigid vegetation canopies but not within flexible
 328 canopies. These observations agree with the velocity structures as proposed in Pujol et al. [39].
 329 However, Luhar et al. [26] and Abdolhahpour et al. [1] also observed wave-driven currents within
 330 flexible vegetation canopies. Their experiment setup differed significantly from ours as they used
 331 blades instead of cylinders. Furthermore, their experiments considered different wave conditions,
 332 longer canopies ($L_v = 3\text{-}9 \text{ m}$) and increased test durations (6-10 min), which may have promoted
 333 flow convergence. Yet, Pujol et al. [39] did not observe wave-driven currents through flexible
 334 canopies over equally long timeframes. Also, our canopy length and test duration sufficed for the
 335 development of currents through rigid vegetation. Given the contrasting observations and
 336 conditions, future research in this topic and its effect on plant motion and associated wave damping
 337 is advised.

338
 339 *Table 1: List of tested wave conditions and damping coefficients for rigid and flexible vegetation. u_c is derived from
 340 measured velocities according to Eq. 3. The width of the 95% CI of β_{exp} is given in brackets after its value. * Based on 2
 341 instead of 3 runs; † Based on 1 run; Data quantity was reduced by control runs (u_c , rigid), or instrument malfunctioning. ‡
 342 Plant motion not captured due to a moving floor plate.*

Case	H [m]	T [s]	h [m]	Rigid vegetation				Flexible vegetation			
				u_c [m/s]	Ca	L	β_{exp} [$10^{-3}/\text{m}$]	u_c [m/s]	Ca	L	β_{exp} [$10^{-3}/\text{m}$]

R1	0.15	1.4	0.60	0.13 [†]	0.02	11	42 (6)	0.15	178	8.9	20 (9)*
R2	0.15	1.6	0.60	0.15*	0.04	7.6	38 (4)	0.19	278	6.2	16 (3)*
R3	0.15	1.8	0.60	0.17*	0.04	6.3	49 (9)	0.20	326	5.1	23 (5)*
R4	0.15	2.0	0.60	0.18*	0.05	5.3	42 (16)	0.22*	390	4.2	15 (16)*
R5	0.10	1.8	0.60	0.11*	0.02	9.2	39 (8)	0.14	146	7.6	20 (8)*
R6	0.20	1.8	0.60	0.21*	0.07	4.9	63 (9)	0.25	498	4.1	26 (19)*
R11	0.15	1.4	0.50	0.17*	0.04	7.9	72 (10)	0.19	271	7.2	21 (7)
R12	0.15	1.6	0.50	0.20*	0.06	6.0	67 (8)	0.21	352	5.5	17 (8)*
R13	0.15	1.8	0.50	0.20*	0.06	5.2	80 (18)	0.23	411	4.6	32 (6)
R14	0.15	2.0	0.50	0.22*	0.08	4.2	70 (30)	0.25	472	3.8	24 (12)
R15	0.10	1.8	0.50	0.14*	0.03	7.4	59 (18)	0.16	191	6.7	26 (5)
R16	0.20	1.8	0.50	0.26*	0.10	4.1	94 (22)	0.30	692	3.5	25 (15)
R21	0.15	1.4	0.40	0.20*	0.06	6.9	145 (23)	0.23	397	6.0	27 (15)
R22	0.15	1.6	0.40	0.21*	0.07	5.5	125 (13)	0.25	507	4.6	28 (13)
R23	0.15	1.8	0.40	0.22*	0.07	4.8	138 (9)	0.27	556	3.9	22 (9)*
R24 [‡]	0.15	2.0	0.40	0.23*	0.08	4.1	108 (4)	0.25	498	3.7	48 (10)
R25	0.10	1.8	0.40	0.16*	0.04	6.7	97 (7)	0.18*	240	6.0	22 (12)*
R26	0.12	1.8	0.40	0.18*	0.05	5.8	116 (9)	0.21*	355	4.9	32 (14)*
R31	0.10	1.4	0.30	0.16*	0.04	8.6	210 (19)	0.18	266	7.3	56 (16)
R32	0.10	1.6	0.30	0.16*	0.04	7.3	219 (32)	0.20	309	5.9	68 (28)
R33	0.10	1.8	0.30	0.18*	0.05	5.9	197 (9)	0.21	333	5.1	62 (19)
R34	0.10	2.0	0.30	0.17*	0.04	5.6	195 (9)	0.20	325	4.6	62 (9)
R35	0.08	1.8	0.30	0.14*	0.03	7.5	169 (6)	0.17	238	6.0	51 (20)
R36	0.12	1.8	0.30	0.20*	0.06	5.3	219 (27)	0.24	444	4.4	40 (11)

343

344

345

346

347

348

349

350

351

352

353

354

355

356

357

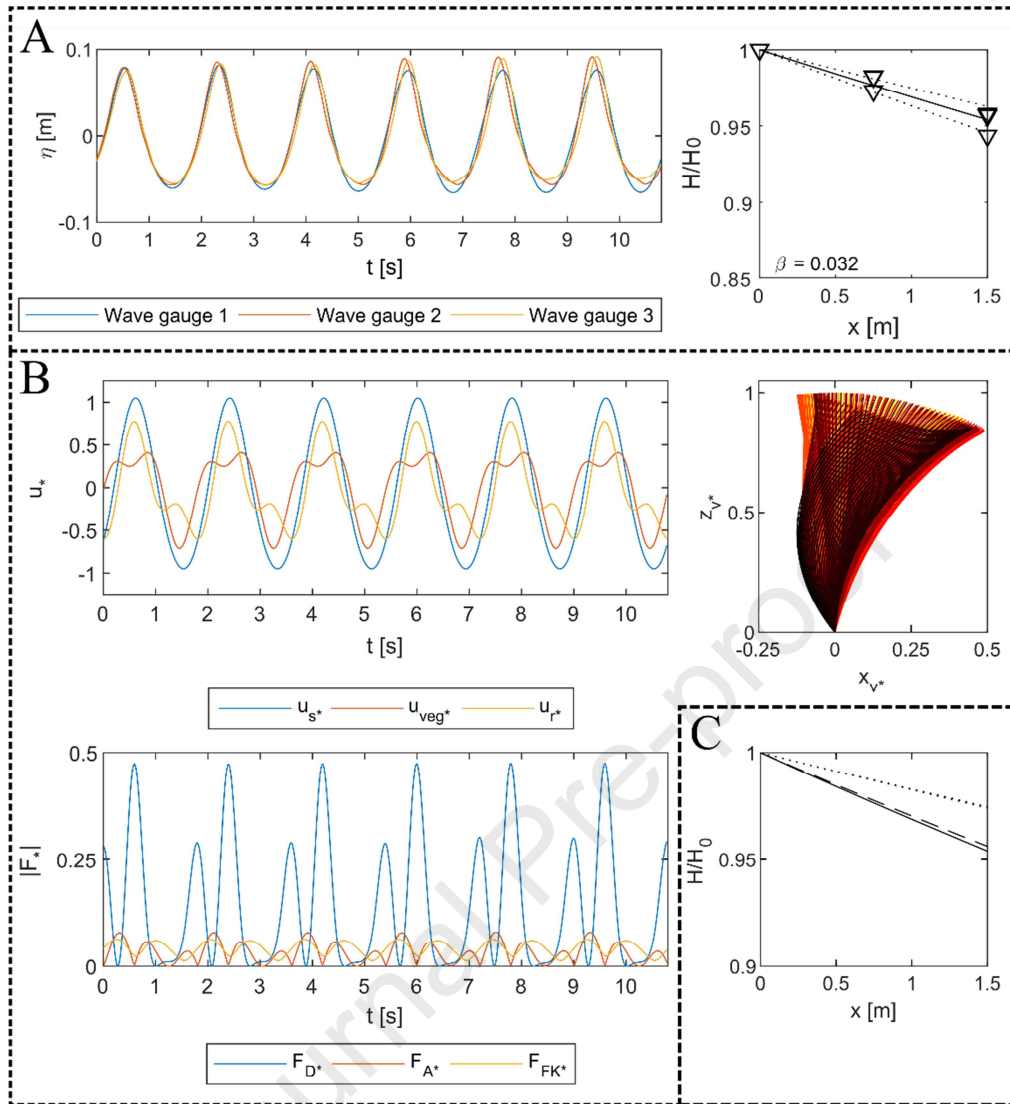
358

359

360

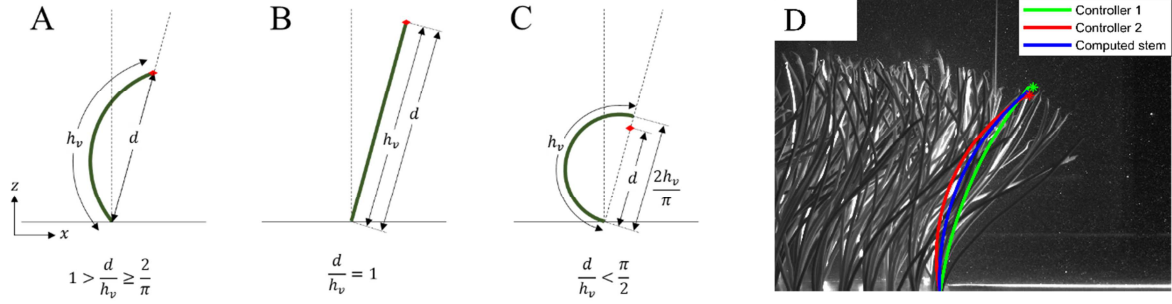
361

Plant motion of flexible vegetation was derived from the frames captured by the PIV-camera through fitting a circular arc between the tip and the root for each frame (Fig. 4). We assume stem inextensibility such that the arc length equals vegetation height, and downstream bending as this is the dominant direction under extreme motion [41]. Under these assumptions, the stem position has a unique solution when the chord length d between the tip and the root satisfies $1 > d/h_v \geq 2/\pi$ (Fig. 4a). If $d = h_v$, a straight stem between root and tip is fitted (Fig. 4b). Finally, a circular arc cannot be fitted when $d/h_v < 2/\pi$, which may occur under extreme bending. The smallest semi-circle with diameter $d = 2h_v/\pi$ is fitted instead (Fig. 4c). Tip positions of a stem at the downstream edge of the patch have been identified manually for each frame by two independent controllers (Fig. 4d). This was found to be more accurate than automatic identification due to the variation in illumination and the low contrast between stems in the canopy. It is noted that a circular arc may not accurately represent stem configurations with two inflection points nor configurations with an arc angle greater than that associated with a semicircle, but it does accurately represent the motion of the tip which sways the most and is identified directly. Additionally, the errors in plant posture may have a limited impact on wave damping as we will show in the following sections. An example of the computed plant motion is included in Figure 3b. Full videos of derived plant motion are included in the supplementary materials.



362
 363 *Figure 3: Schematic diagram of the data collection from (A) wave gauges and (B) PIV, and (C) comparison of β under*
 364 *conditions R13 with flexible vegetation. Top left: time series of the water surface elevation as measured by the three*
 365 *wave gauges and corrected for phase differences. Top right: the data of the three repeats (triangles, some data points are*
 366 *overlapping) is combined to fit β_{exp} (solid line) with 95% confidence interval (dotted lines). Middle left: PIV derived*
 367 *horizontal particle velocities, vegetation velocity and relative velocity at $s_* = 0.5$. Middle right: PIV-derived plant motion.*
 368 *The colouring denotes the time and ranges from yellow (start of run) to black (end of run). Bottom left: Magnitudes of the*
 369 *wave forces at $s_* = 0.5$. Bottom right: Comparison of the force-derived β_{for} (dashed line) with β_{exp} (solid line). The dotted*
 370 *lines (only one is visible due to overlapping) denote β_{for} of the other repeats of R13.*

371 The observed plant motion ranged from straight stems to fully flattened canopies. Plant motion
 372 developed during the measurement period with 25% of the runs exhibiting a change in maximum
 373 bending angle of more than 10° . It is expected that this affected the measured wave damping and
 374 the wave forces equally. The vegetation velocity is derived numerically through a central difference
 375 scheme on the plant configuration. Following the derivation of water particle velocities, we have
 376 applied a Fourier filter to retain only the natural and first order harmonics of the vegetation velocity.
 377

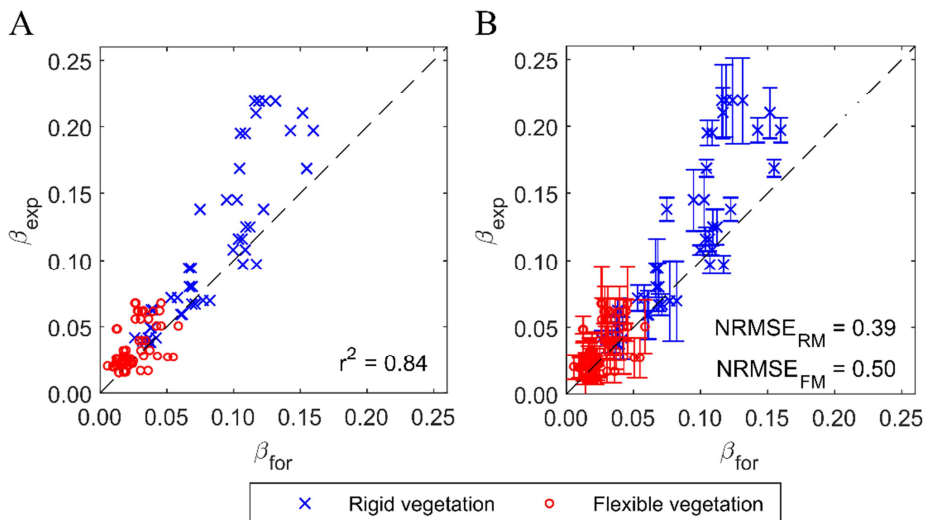


378 Figure 4: Schematisation of the derivation of the plant position from a fixed root and identified tip position (red diamond)
 379 under three conditions: (A) a bent stem, (B) a straight stem and (C) extreme stem bending; and (D) application to a sample
 380 image.

381 The wave-induced forces are computed based on the velocity signal and plant motion, according to
 382 Eq. 6-8 (Fig. 3B). Then, the force-derived damping coefficients β_{for} was solved numerically through
 383 substitution of Eq. 15 in Eq. 12 (Fig. 3C). This produces a third-order polynomial function which may
 384 provide three instead of one solution for β_{for} . In these instances, the β_{for} which is closest to β_{exp} is
 385 selected. β_{for} successfully reproduces the wave damping over flexible vegetation an order of
 386 magnitude smaller than over rigid vegetation with goodness-of-fit $r^2 = 0.84$ (Fig. 5), using a drag
 387 coefficient that was derived for rigid vegetation. This shows that explicitly including the plant motion
 388 effect in the drag force (Eq. 6) can explain the reduction in wave damping by flexible vegetation.

389
 390 Whilst the confidence interval in β_{exp} has been quantified from the water surface measurements,
 391 this was not possible for β_{for} . Therefore, we here address the individual sources of error in β_{for} ,
 392 namely: the C_d -relation (Eq. 9), the velocity measurements, and the plant motion. Eq. 9 was fitted
 393 with a goodness-of-fit of $r^2 = 0.89$ (Hu, pers. comm.), but a confidence interval is not known. The
 394 normalized standard deviation of the measured velocity amplitude (Eq. 2) at identical water depth
 395 and vegetation type varied between 0.02 and 0.08. Thirdly, the normalized standard deviation of the
 396 vegetation velocity ranged between 0.12 and 0.25 at the tip. Each error propagates into β_{for} , which
 397 contributes to the scatter of data seen in Fig. 5. The normalized root-mean-square errors (NRMSE) of
 398 β_{for} with respect to β_{exp} are 0.39 and 0.50 for rigid and flexible vegetation respectively. Whilst the
 399 r^2 of our methodology is very good, the fit may improve further with data from additional wave
 400 gauges to estimate β_{exp} more accurately, or when the uncertainty by any of the model errors is
 401 mitigated which can be recommended for future studies.

402



403
 404 Figure 5: (A) The correlation between the force-derived damping coefficient β_{for} and the measured damping coefficient
 405 β_{exp} , and (B) same as (A) with error bars that match the 95% confidence interval of β_{exp} . The normalized root-mean-square
 406 error (NRMSE) is given separately for the rigid (RM) and flexible (FM) mimics.

3.2 Key mechanisms in the wave-vegetation interaction

407

408

409

410

411

412

413

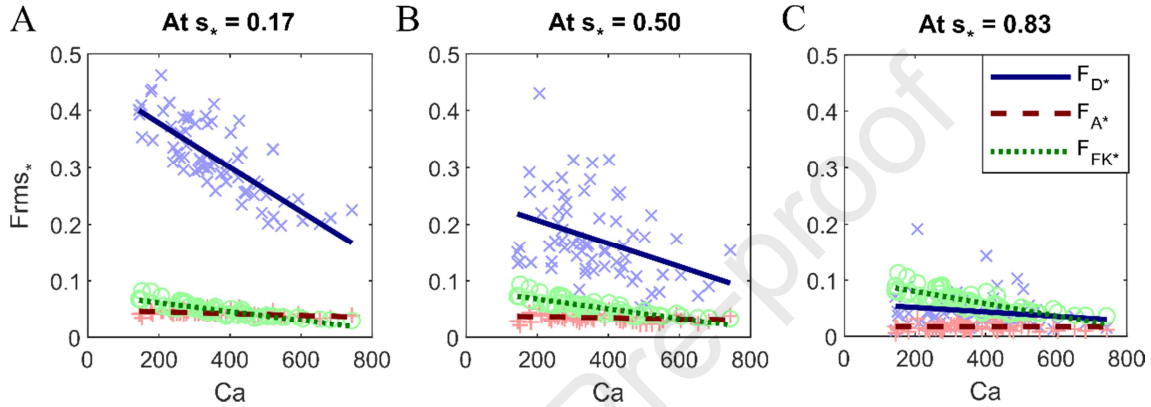
414

415

416

417

418



419

420

421

Figure 6: Root-mean-square force magnitude of the drag force F_{D*} , the added mass force F_{A*} , and the Froude-Krylov force F_{FK*} on flexible vegetation as function of the Cauchy number at (A) $s_* = 0.17$, (B) $s_* = 0.5$, and (C) $s_* = 0.83$.

422

423

424

425

426

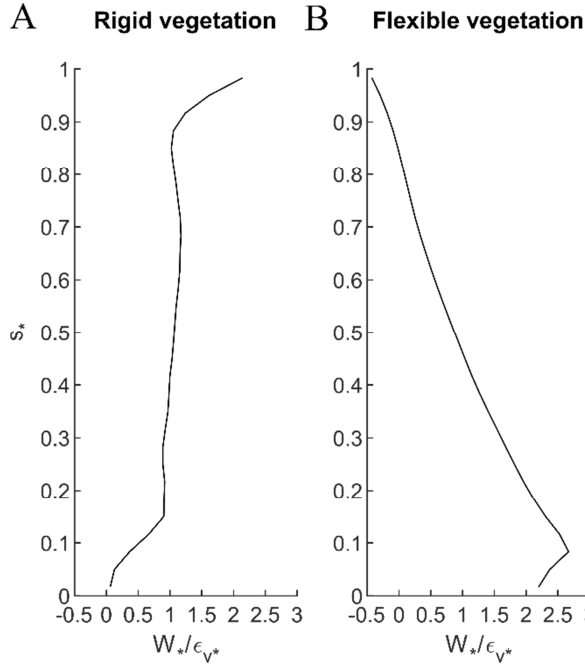
427

428

429

430

Distribution of wave energy dissipation: The distribution of energy dissipation versus stem length shows that most energy is dissipated where the stem is upright and its motion is minimal (Fig. 7). The dissipation over an upright rigid stem is approximately constant along its length with a peak in dissipation at the tip where amplified velocities were observed due to wave-driven currents through the top of the canopy [see e.g. ,1,39]. Alternatively, the wave dissipation is concentrated at the bottom part of the stem for flexible vegetation with near-zero to negative contributions at the top section ($s_* > 0.7$). The decreasing contribution to energy dissipation over the stem length is inversely proportional to stem motion, which is absent at the fixed root and maximum at the tip.



431
432 Figure 7: Average rate of energy dissipation against the along-stem coordinate for (A) rigid and (B) flexible vegetation.

433 *Stem reconfiguration versus stem velocity:* The swaying of flexible vegetation reduces wave damping
 434 in two ways. First, reconfiguration of the stem posture reduces the stem frontal area [38] and
 435 modifies the direction of wave forces [29,50]. Second, stem velocity reduces the relative velocity
 436 between stem and water [e.g. 32]. Both mechanisms reduce the work done by the drag force but
 437 have not been quantified individually. To identify the dominant mechanism, we quantify β by
 438 modifying Eq. 6 such that it solely includes stem reconfiguration or stem velocity. Wave damping by
 439 stem reconfiguration includes the directionality of the drag force relative to the stem, but the
 440 vegetation velocity is set at zero such that
 441

$$F_{D_*} = \frac{1}{2} C_D |u_{n_*}| u_{n_*} e^{-i\theta} \quad (16)$$

442
 443 with u_{n_*} as the stem-normal component of the water velocity. Alternatively, stem velocity includes
 444 the relative velocity in the force equations, but the stem is considered upright for the directionality
 445 of the forces, i.e.
 446

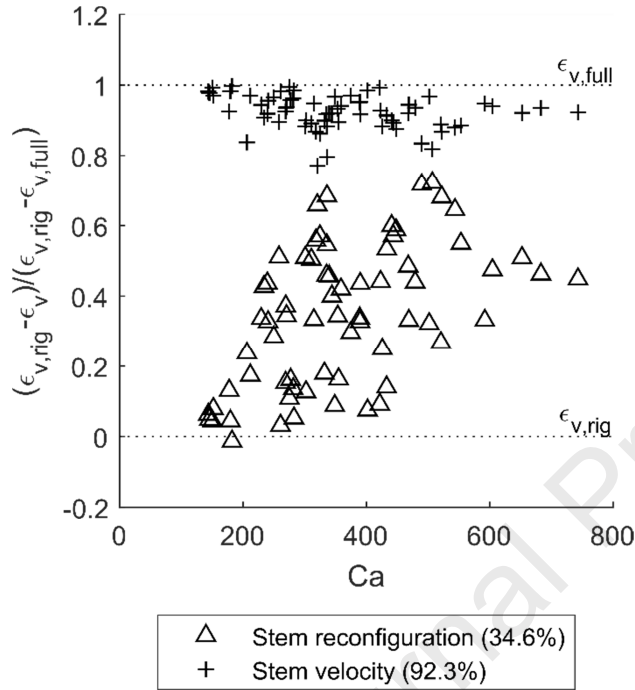
$$F_{D_*} = \frac{1}{2} C_D |u_{r_*}| u_{r_*} \quad (17)$$

447
 448 Finally, we consider the rigid stem drag force which excludes both stem reconfiguration and stem
 449 velocity as a reference for the relative contribution of each mechanism. The rigid stem drag force is
 450 given by
 451

$$F_{D_*} = \frac{1}{2} C_D |u_{s_*}| u_{s_*} \quad (18)$$

452
 453 The respective wave damping coefficients are obtained as described in Section 3.1. The
 454 contributions of the bending (Eq. 16) and relative velocity (Eq. 17) to wave damping are scaled
 455 against the damping that is simulated by the full drag force equations (Eq. 6) and the damping
 456 simulated by the rigid stem drag force (Eq. 18).
 457

458 Our results show that stem velocity is more important than stem reconfiguration. The inclusion of
 459 stem velocity explains 92.3% of the observed reduction in ϵ_v due to plant motion, whereas the
 460 individual contribution of the stem reconfiguration is 34.6% (Fig. 8). Thus, the stem velocity effect
 461 can explain almost all reduction in wave energy dissipation. Conversely, whilst stem bending can
 462 explain 34.6% of the reduction in wave energy dissipation individually, its added effect when the
 463 relative velocity is included is only 7.7%. These results fit with the concentration of energy
 464 dissipation at the lower section of the stem (Fig. 7), which is straighter than the top section. Stem
 465 bending is significant at the tip, but the contribution of the top section to wave energy dissipation is
 466 small.
 467



468
 469 *Figure 8: Individual contributions of stem reconfiguration (based on Eq. 16) and stem velocity (based on Eq. 17) effects to*
 470 *the reduction in the wave energy dissipation. The average contribution of each effect is given between brackets. The*
 471 *contributions are scaled relative to the energy dissipations based on the full drag force (Eq. 6, upper dotted line) and the*
 472 *drag force based on a rigid stem (Eq. 18, lower dotted line).*

473

474 4. Model for wave damping over flexible vegetation

475

476 4.1 Model assumptions

477

478 The key mechanisms in the wave-vegetation interaction justify our assumptions for modelling wave
 479 damping of regular waves over flexible vegetation. We assume that

- 480 1. Wave energy is dissipated where plant deflections are small and the plant posture is near-
 481 vertical;
- 482 2. The drag force controls the wave-vegetation interaction;
- 483 3. Stem-stem interactions can be neglected;
- 484 4. Vegetation is cylindrical with homogeneous cross-sections and flexural rigidity;
- 485 5. Stems are inextensible.

486

487 Assumption 1 is supported by the concentration of energy dissipation in the upright lower part of a
 488 flexible stem and the dominant contribution of the relative velocity mechanism relative to stem
 489 bending, as supported by our experiments. Assumption 2 follows from the observation that F_{A*} and
 490 F_{FK*} are an order of magnitude smaller than F_{D*} in the bottom section of the stem which is key for

491 wave damping. F_{A^*} and F_{FK^*} may be important at the top sections of a flexible stem but their
 492 magnitude remains an order of magnitude smaller than F_{D^*} in the bottom section. Assumptions 3-5
 493 are required to derive the force balance (Eq. 11), which was successfully applied to predict wave
 494 forces.

495
 496 Our model assumptions reflect those in small excursion models as in Méndez et al. [33] and
 497 Mullarney and Henderson [35], who used Euler-Bernoulli beam theory to solve vegetation motion.
 498 Here we have provided new experimental support for this type of model, but our model differs in
 499 the extension of plant motion to wave damping. Scaling analysis shows that small excursion models
 500 are valid for $L \gg 1$ [29]. Our experimental results ($L = 3-9$) show that the wave energy dissipation is
 501 concentrated at the bottom section of a stem where its velocity and excursion are low compared to
 502 the water velocity. This suggests that the model assumptions are valid for excursion ratios in the
 503 order $O(10^0)$. The model validation (Section 5.2) includes wave and vegetation conditions with L as
 504 low as 1.4 which covers most salt marsh ($L = 0.3-10$, [41,47]) and sea grass ($L = 0.5-6$, [22])
 505 conditions. In case of $L < 1$, flexible vegetation may be fully extended, and the vegetation velocity
 506 may reduce to 0. Under these conditions, our model will provide a conservative estimate of the
 507 energy dissipation. Furthermore, we have considered vegetation conditions up to $Ca \approx 700$ in our
 508 experiments. The dominance of F_D on the bottom stem section is well established by our
 509 experimental evidence within this range, but may not be extrapolated to more flexible vegetation.
 510 The conditions $L > 1.4$ and $Ca < 700$ represent the quasi-flexible vegetation conditions for which
 511 our model will be validated. Finally, the model is derived for cylindrical vegetation but it can easily
 512 be extended to other plant geometries given appropriate relations for C_D and Ca .

513 514 4.2 Solution of plant motion

515
 516 Under the model assumptions, vegetation motion is governed by horizontal stem excursion (x_{v^*})
 517 which must satisfy the force balance (Eq. 11) in the horizontal direction. For a near-vertical stem, it is
 518 appropriate to scale x_v by the horizontal water particle excursion length A_w rather than by plant
 519 length h_v as was done up to this point, i.e. $x_{v^*} = x_v/A_w$ and $u_{veg^*} = \partial x_{v^*}/\partial t_*$. Furthermore, the
 520 bending angle is approximated as $\theta \approx \partial x_{v^*}/\partial z_{v^*}$ and $s_* \approx z_{v^*}$ at this small-deflection limit [29,35].
 521 We consider thin stems for which stem inertia is negligible ($\frac{1}{2} \frac{\pi^2}{KC} \rho' \ll 1$). Finally, the drag force, now
 522 given by Eq. 17, is linearised for the purpose of solving the force balance only. Under these
 523 conditions, Eq. 11 simplifies as

$$524 \quad \frac{\partial^4 x_{v^*}}{\partial z_{v^*}^4} = Q \left(u_{s^*} - \frac{\partial x_{v^*}}{\partial t_*} \right) \quad (19)$$

525
 526 where $Q = \frac{4}{3\pi} C_D CaL \int_0^1 (a_u - a_v) dz_{v^*}$ is the linearised parameterisation of the magnitude of drag
 527 force, and a_u and a_v are the amplitudes of the water and vegetation velocity respectively.
 528 Equivalent work is done over a wave cycle by the linearised drag as would be by quadratic drag [e.g.
 529 33,51]. The boundary conditions of Eq. 19 are defined as clamped at the root, $x_{v^*} = \partial x_{v^*}/\partial z_{v^*} = 0$
 530 at $z_{v^*} = 0$, and free at the tip, $\partial^2 x_{v^*}/\partial z_{v^*}^2 = \partial^3 x_{v^*}/\partial z_{v^*}^3 = 0$ at $z_{v^*} = 1$.

531
 532 Wave and plant motion are periodic over a wave cycle and must satisfy the eigenvalue problem
 533 posed by Eq. 19. Therefore, we separate the motion quantities in a temporal mode following the
 534 monochromatic wave frequency and orthogonal spatial modes following the given eigenvalue
 535 problem [35], according to

$$536 \quad u_{s^*} = \Re \left(e^{it_*} \sum_{n=1}^{\infty} U_n \psi_n \right), \quad u_{veg^*} = \Re \left(e^{it_*} \sum_{n=1}^{\infty} V_n \psi_n \right), \quad x_{v^*} = \Re \left(e^{it_*} \sum_{n=1}^{\infty} X_n \psi_n \right). \quad (20)$$

537

538 The spatiotemporal complex coefficients U_n , V_n and X_n denote the weights of each mode in spectral
 539 space. The spatial modes ψ_n satisfy $\partial\psi_n/\partial z_{v^*} = \alpha_n\psi_n$ where α_n are the eigenvalues of each spatial
 540 mode. Further details regarding the structure of ψ_n are provided in Appendix A.

541

542 By substitution of Eq. 20 in Eq. 19 and summation over all spatial modes, we construct the transfer
 543 function $T = a_T e^{i\phi_T}$ between the water and stem motion in physical space according to

544

$$V_f = T U_f \quad (21)$$

545

546 where $U_f(z_{v^*}) = \sum U_n \psi_n = a_u e^{i\phi_u}$ and $V_f(z_{v^*}) = \sum V_n \psi_n = a_v e^{i\phi_v}$ are complex temporal
 547 coefficients in physical space, and

548

$$T = \frac{\sum \left(\frac{U_n \psi_n}{1 - \frac{i\alpha_n^4}{Q}} \right)}{\sum U_n \psi_n}. \quad (22)$$

549

550

551 Here, a_T denotes amplitude transfer from water to stem motion and ϕ_T denotes the phase lag
 552 between water and stem motion. As Q is a function of a_v , Eq. 22 is solved iteratively. There is a
 553 unique solution as shown in Appendix B. The numerical implementation expands velocity structures
 554 to 10 spatial modes as additional modes did not change the resulting transfer function.

555

556 Additionally, we define the transfer function $B = a_b e^{i\phi_b}$ between water velocity and relative
 557 velocity, i.e. $U_f - V_f = B U_f$. By substitution of this definition in Eq. 21, it follows

558

$$B = 1 - T. \quad (23)$$

559

560 4.3 Work factor (χ)

561

562 To include the effects of plant motion on energy dissipation, we define z_{v^*} -dependent work factor

563

$$\chi(z_{v^*}) = \frac{\bar{W}_*}{\bar{W}_{rig*}}, \quad (24)$$

564

565 such that

566

$$\epsilon_{v^*} = \int_{z_{v^*}=0}^1 \chi \bar{W}_{rig*} dz_{v^*}, \quad (25)$$

567

568 where \bar{W}_* is the phase-averaged work done over a flexible stem and \bar{W}_{rig*} is the work done over a
 569 rigid stem with equal dimensions. By substitution of Eq. 17, 23 in Eq. 14, the phase-averaged work
 570 done by the drag force on a stem is given by

571

$$\bar{W}_* = \frac{1}{4\pi} C_D \int_{t_*=0}^{2\pi} |\Re(BU_f e^{it_*})| \Re(BU_f e^{it_*}) \Re(U_f e^{it_*}) dt_*. \quad (26)$$

572

573 We note that $\Re(e^{it_*}) = \cos t_*$ and set $\phi_u = -\phi_b$ without loss of generality as W_* is averaged over a
 574 wave cycle. Then, Eq. 26 reduces to
 575

$$\overline{W}_* = \frac{2}{3\pi} C_D a_b^2 a_u^3 \cos \phi_b. \quad (27)$$

576
 577 In case of rigid vegetation, $a_b = 1$ and $\phi_b = 0$ as velocity transfer is absent, such that
 578

$$\overline{W}_{rig*} = \frac{2}{3\pi} C_D a_u^3 \quad (28)$$

579
 580 and, by substitution of Eq. 27, 28 in Eq. 24,
 581

$$\chi = a_b^2 \cos \phi_b. \quad (29)$$

582
 583 Eq. 29 shows how the velocity transfer controls wave damping. Changes in amplitude and phase of
 584 the relative velocity directly affect the work done by waves on vegetation and, thereby, the wave
 585 damping. Defining χ is computationally more efficient than computing the vegetation and relative
 586 velocity time series.

587 588 **4.4 Wave damping**

589
 590 A formulation for wave damping coefficient β_* is obtained by substitution of Eq. 15, 25 in Eq. 12,
 591 which leads to
 592

$$\frac{\beta_*}{(1 + \beta_* \chi_*)^3} = 4 \frac{\lambda_f F_r^2}{D c_{g*} H_{0*}^2} \int_{z_{v*}=0}^1 \chi \overline{W}_{rig*} dz_{v*}. \quad (30)$$

593
 594 Eq. 30 represents a third-order polynomial which is solved numerically. There may be up to three
 595 roots that satisfy Eq. 30, of which the root closest to the estimate by linear wave theory (Eq. 32,
 596 Section 4.5) is selected.

597 598 **4.5 Wave damping under linear wave theory**

599
 600 When the validity of linear wave theory inside the canopy is assumed, the velocity structure is
 601 controlled by the ambient velocity field. The amplitude of the water particle velocities is given by
 602

$$a_u(x_*, z_{v*}) = \frac{H_* k_* \cosh Lk_* z_{v*}}{2F_r^2 \cosh Dk_*}. \quad (31)$$

603
 604 Substitution of Eq. 15, 28, 31 in Eq. 30 and application of the dimensionless dispersion relation
 605 $DF_r^2 = k_* \tanh(Dk_*)$ reduce the conservation of energy to a single expression for β_* , according to
 606

$$\beta_* = \frac{4}{3\pi} C_D \lambda_f D k_*^2 H_{0*} \frac{\int_{z_{v*}=0}^1 \chi \cosh^3(Lk_* z_{v*}) dz_{v*}}{(\sinh 2Dk_* + 2Dk_*) \sinh Dk_*}. \quad (32)$$

607
 608 We note that for rigid vegetation, $\chi = 1$ and Eq. 32 reduces to the rigid vegetation solution provided
 609 in Dalrymple et al. (1984).

610 611 **5. Model validation**

612

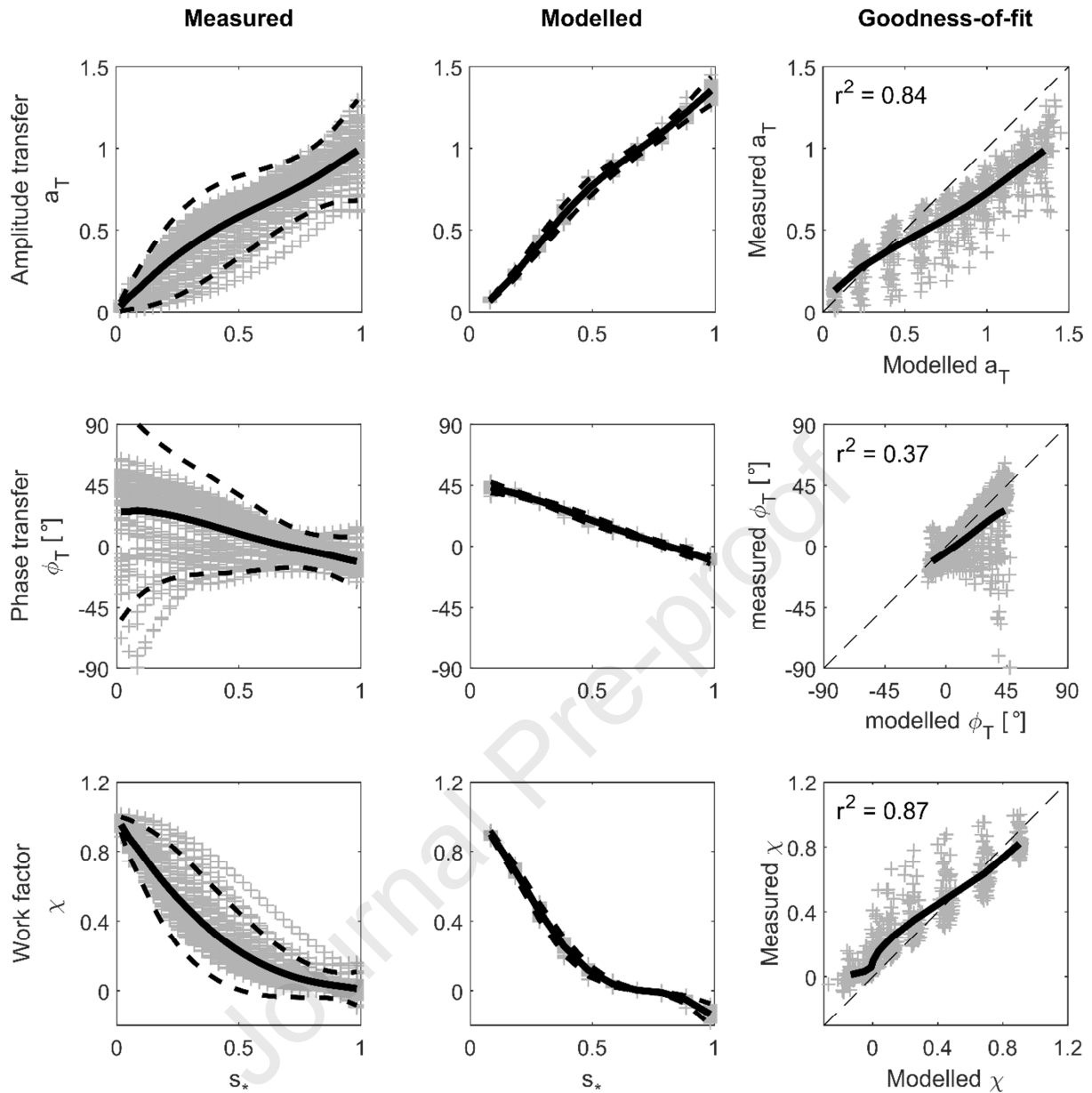
5.1 Validation of the velocity transfer function (T)

The modelled velocity transfer function T is validated against a measured transfer function based on the observed water and plant motion. The measured transfer function is derived from the amplitude and phase differences in the natural harmonic of the observed water particle and stem velocities (Section 3.1). The validation includes flexible vegetation only, as the transfer function for rigid vegetation is trivial.

The amplitude a_T of the transfer function is excellently reproduced by the model (Fig. 9, top row). The amplitude transfer is $a_T \approx 0$ at the root where the stem is clamped and increases towards the tip to $a_T \approx 1$ for both measured and modelled transfer functions. This indicates that the tip closely follows the water motion and the relative velocity is small, which fits with observations that the energy dissipation is small at the tip. The coefficient of determination is excellent with $r^2 = 0.84$. The velocity transfer is slightly overpredicted at the tip where the assumption of a near-vertical stem affected only by the drag force may not hold. Additionally, the modelled transfer function is steady state, but the measured transfer function was still developing in a quarter of the runs. In these cases, the measured transfer function is lower than the steady-state function, which may also contribute to the over-prediction of the modelled transfer function at the tip. The transfer function at the bottom section of the stem which is important for wave damping is modelled correctly.

The phase ϕ_T is reproduced well for most experimental runs (Fig. 9, middle row). Both measured and modelled phases show that the stem velocities lead water motion by 45° at the root, which decreases towards the tip where the water motion leads stem motion by 10° . The scattering of experimental data is larger than predicted by the model due to natural variation in wave-vegetation interaction not captured by the model and measurement errors in water and vegetation motion. The scattering is maximum at the root where stem motion is minimal and, therefore, phase calculations are most sensitive to measurement errors. A limited number of outliers (10 out of 68 successful runs) impact the coefficient of determination negatively ($r^2 = 0.37$). Yet, a visual comparison shows that most data points are centred around the line of perfect fit.

Work factor χ is excellently reproduced by the model (Fig. 9, bottom row). The measured work factor is derived from the measured transfer function via Eq. 29. The work done by waves on a flexible stem at the root is equal to the work done on a rigid stem as denoted by $\chi = 1$ at $s_* = 0$. The work factor decreases as the amplitude transfer from water to stem motion increases from root to tip. Here, a negative χ indicates that the stem velocities locally exceed the water velocities and the relative velocity is fully out of phase with the water velocities. This behaviour agrees with Mullarney and Henderson [35] who showed that the tip motion of flexible stems can exceed the water motion that forces it. The agreement between measured and modelled work factors is excellent with $r^2 = 0.87$.



653
654
655
656
657
658

Figure 9: Validation of the velocity transfer function between water and stem motion. Top row: amplitude transfer a_T ; middle row: phase transfer ϕ_T ; bottom row: work factor χ . The thick line denotes the mean of the measured (left column) or modelled (middle column) transfer functions, or the goodness-of-fit of the mean (left column). The dashed lines denote the 95% observation interval (mean \pm 2 standard deviations), or the line of perfect fit (left column). The grey + signs represent individual observations.

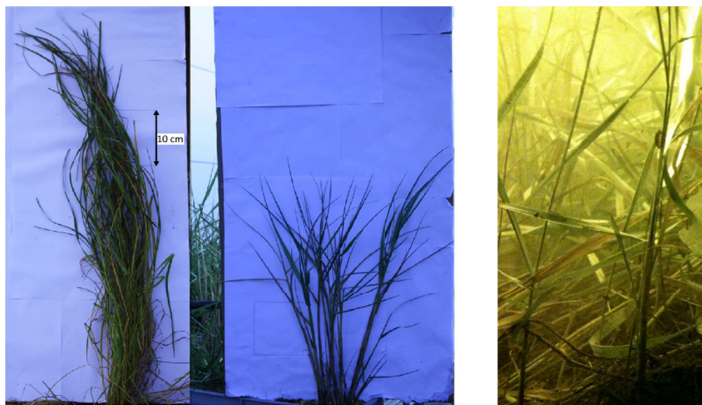
659
660
661

5.2 Validation of the damping coefficient

662 Damping coefficient β is validated across five vegetation species with distinct biomechanical
663 properties under medium and high energy wave conditions. These include wave damping by the
664 rigid and flexible artificial vegetation (Section 3.1) and against three species of real salt marsh
665 vegetation: *Spartina Anglica*, *Puccinellia Maritima* and *Elymus Athericus* (Fig. 10). These species
666 differ in dimensions and flexural rigidity (Table 2) and have been tested under regular waves in large-
667 scale flumes. The test conditions varied in water depth, wave height, wave period and stem density
668 such that the model is validated across a wide range of wave and vegetation conditions.
669

670 *S. Anglica* and *P. Maritima* were tested in the Cantabria Coastal and Ocean Basin (CCOB) of the
671 University of Cantabria, Spain [19,24,31]. *S. Anglica* is a stiff plant with the largest diameter of the

672 species tested. Alternatively, *P. Maritima* is a thin and flexible salt marsh grass. The experimental
 673 conditions featured medium water depths ($h = 0.4 - 0.6$ m) and wave heights ($H = 0.15 - 0.20$ m)
 674 at a range of wave periods ($T = 1.2 - 2.2$ s) and vegetation densities ($n_v = 430 - 2436$ stems/m²).
 675



676 *P. Maritima*

677 *S. Anglica*

678 *E. Athericus*

679 Figure 10: The three real vegetation species that were used for model validation. Photo of *P. Maritima* and *S. Anglica* is
 680 adapted from Lara et al. [19]. Photo of *E. Athericus* is provided through the courtesy of Iris Möller (no scale available).

681 *E. Athericus* was tested in the Grosser Wellenkanal (GWK) of Forschungszentrum Küste in Hannover,
 682 Germany [34,41]. *E. Athericus* is a thin and tall semi-flexible salt marsh grass. A 40 m long vegetation
 683 field was submerged in deep water ($h = 2$ m) and subjected to medium and high energy wave
 684 conditions ($H = 0.11 - 0.89$ m, $T = 1.5 - 5.1$ s). The stem density decreased as the experiments
 685 progressed due to stem breaking. Therefore, the model was run following stem density data
 686 provided in Rupprecht et al. [41].

687 The model is run with plant and wave conditions of individual runs as input. It is assumed that wave
 688 damping by real vegetation is dominated by the cylindrical stems. Fig. 10 shows that the geometry of
 689 the tested *S. Anglica* and *P. Maritima* species is dominated by their stems, and the tested *E.*
 690 *Athericus* was considered cylindrical in Rupprecht et al. [41]. The velocity fields around real
 691 vegetation are based on linear wave theory (Section 4.5), which was also successfully applied in the
 692 wave damping analysis in Losada et al. [24] and Möller et al. [34]. The drag coefficient for all species
 693 is given by Eq. 9. The velocity scale is based on linear wave theory halfway based on measured wave
 694 height halfway the vegetation field as an estimate of the spatially averaged velocity. This non-
 695 predictive definition of the velocity scale can be avoided if the vegetation field is divided into
 696 sufficiently short sections, as is typically done when calculating vegetation-induced wave damping in
 697 large-scale computational wave models that use a gridded computational domain [e.g. SWAN, 4].

698 The agreement between modelled and measured wave damping is good with $r^2 = 0.66$ (Fig. 11),
 699 which shows that our model is applicable across a range of plant and wave conditions without plant-
 700 specific calibration. Excellent agreement is obtained for rigid and flexible artificial vegetation and for
 701 *E. Athericus*. The absence of vegetation motion is correctly modelled for rigid vegetation, as is the
 702 reduction in wave damping by flexible vegetation and *E. Athericus* due to plant swaying. Wave
 703 damping by *S. Anglica* and *P. Maritima* is predicted in the right order of magnitude but with
 704 significant scattering of the data, as demonstrated by their NRMSE of 0.56 and 0.62 respectively.
 705 This is partly attributed to the experiment setup of CCOB. Unlike rectangular flumes where
 706 vegetation spans the entire flume width, the CCOB features a circular platform on which vegetation
 707 is positioned. A circular vegetation patch may contribute to wave diffraction and other three-
 708 dimensional hydrodynamic effects, which are not included in our model. Furthermore, our omission
 709 of wave damping by leaves and stem interactions may have contributed to an underestimation of
 710 the measured wave damping, as is observed for *P. Maritima*. Finally, buoyancy, added mass, and

711 Froude-Krylov forces may have initiated a non-passive plant motion, which is not captured by our
 712 model and thus contributes to uncertainty in β_{model} .

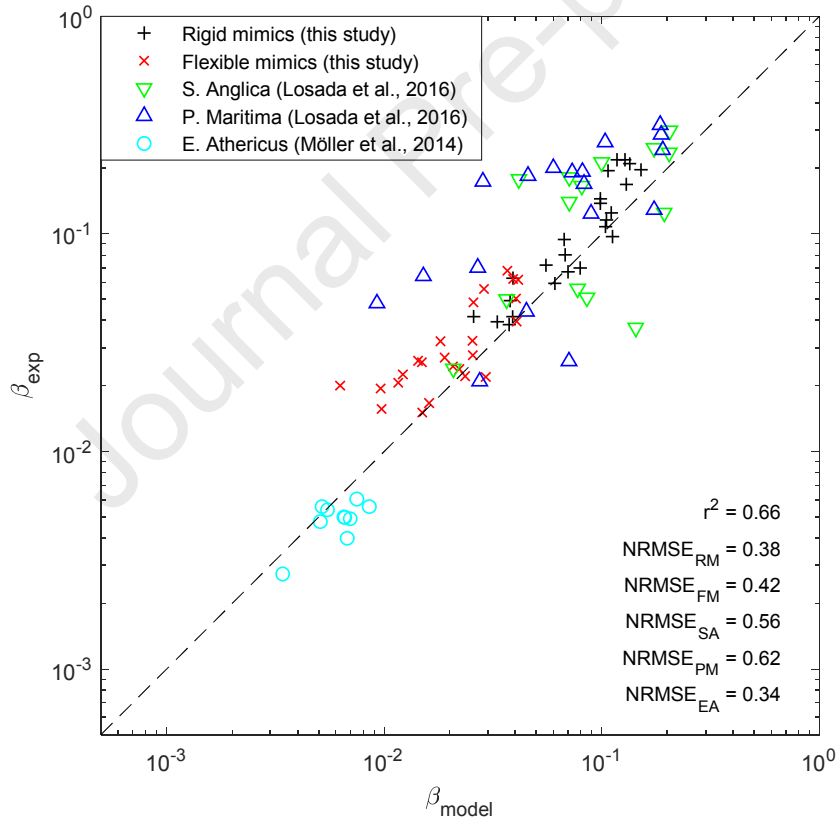
713

714 Table 2: List of vegetation species used for model validation. n denotes the number of unique wave conditions.

Parameter	Rigid mimics	Flexible mimics	<i>S. Anglica</i> [19,24,31]	<i>P. Maritima</i> [19,24,31]	<i>E. Athericus</i> [34,41]	Unit
Type	Artificial	Artificial	Real	Real	Real	-
h_v	300	300	284	473	700	mm
b_v	5.0	5.0	6.0	3.0	1.3	mm
El_v	9.0×10^{-2}	1.7×10^{-5}	1.8×10^{-2}	8.7×10^{-5}	3.0×10^{-4}	Nm ²
n_v	1111	1111	430 - 729	877 - 2436	666 - 1225	m ⁻²
u_c	0.13 - 0.26	0.14 - 0.30	0.16 - 0.33	0.16 - 0.38	0.09 - 0.75	ms ⁻¹
Ca	0.02 - 0.10	146 - 692	0.20 - 0.84	96 - 530	11 - 824	-
L	4.1 - 11	3.5 - 8.9	2.5 - 8.6	4.0 - 13	1.4 - 24	-
Q^*	0.19 - 0.29	1013 - 1601	0.82 - 2.0	1041 - 2314	654 - 1656	-
n	24	24	14	18	10	-

715 * At first iteration, i.e. $a_v = 0$.

716



717

718 Figure 11: Validation of the modelled wave damping coefficients β_{model} against the measured wave damping coefficients
 719 β_{exp} across two types of artificial vegetation and three species of real vegetation. The dashed line denotes a perfect fit. The
 720 r^2 goodness-of-fit is given, as well as the NRMSE of each specie. RM: Rigid mimics; FM: Flexible mimics; SA: *S. Anglica*; PM:
 721 *P. Maritima*; EA: *E. Athericus*.

722

723 6. Conclusions and discussion

724

725 We have developed a mathematical model for the damping of regular waves over coastal vegetation
 726 under quasi-flexible vegetation conditions, based on the key physical processes involved in the

727 wave-vegetation interaction. Three mechanisms were identified during the experimental
728 investigations as important for wave damping over rigid and flexible vegetation: (i) the drag force is
729 the dominant force in the bottom section of a flexible stem; (ii) wave energy is dissipated in the
730 bottom section of a flexible stem; (iii) wave energy dissipation is controlled by the velocity difference
731 between water and stem rather than the reconfiguration of stem posture. We found that the energy
732 dissipation by rigid stems was maximum at the stem tip where the wave velocities were the largest,
733 while the dissipation by flexible stems was maximum at the upright bottom section where stem
734 motion was the smallest.

735

736 Supported by our experimental investigations, we model vegetation as near-vertical flexible rods in
737 which wave damping is controlled by the velocity transfer from water to stem motion. The velocity
738 transfer is linked to a new work factor, which describes the reduction in wave dissipation relative to
739 rigid vegetation due to plant motion. Wave damping in the model is a function of vegetation and
740 wave parameters and does not require the calibration of the drag coefficient for different plant
741 species.

742

743 Our model successfully reproduces wave damping over vegetation for five coastal vegetation
744 species, which differ in geometry and flexural rigidity, and under different wave climates. The model
745 validation included three real vegetation species tested in large-scale experiments. Our model
746 reproduced wave damping in the right order of magnitude for each specie and for both medium and
747 high energy wave conditions, which shows its validity across a wide range of representative field
748 conditions.

749

750 As our model does not require site-specific calibration, it is particularly suited to areas with
751 spatiotemporal variations in vegetation and hydrodynamic conditions. It benefits large areas or
752 areas where interventions such as managed realignment, grazing, and the introduction of new
753 species are considered. Furthermore, the model can be applied to vegetation of different types, sizes
754 and flexibilities when the plant geometry can be represented as a cylinder.

755

756 Despite the potential of our model shown in this research, it is important to emphasize the potential
757 limitations that should be considered in the application of this model. First, the model assumptions
758 rely on the experimental investigations, which limits their applicability to the quasi-flexible
759 vegetation conditions considered in this study, i.e. $L > 1.4$ and $Ca < 700$. These conditions are
760 applicable to most coastal vegetation species, but may be exceeded for very flexible species and
761 during extreme wave conditions. Secondly, wave-vegetation mechanisms like vegetation-induced
762 currents and inertia forces have been omitted in our modelling framework as they were not
763 identified as key processes for wave damping in our experimental vegetation types. Our aim has
764 been to develop a computationally fast model that balances complexity and applicability, justifying
765 our focus only on key mechanisms. However, the selected key processes have been based on a
766 specific set of experiments, which for example showed a negligible impact of wave-driven streaming
767 within flexible vegetation canopies as opposed to other experimental studies [1,26]. Although inertia
768 forces have been included in other wave damping models [e.g. 29,31], we found that they only had
769 limited impact on wave damping in our experiments. Finally, the impact of leaves and stem-stem
770 interactions were not considered in this study. Their influence on wave damping remains an open
771 question.

772

773 Finally, our model builds strongly on our experimental data although we validated wave damping
774 against independent datasets found in literature with real vegetation. The strong tie between
775 experimental work and modelling means that uncertainties in model observations may propagate
776 into model simulations. The main uncertainties in the experimental work are the relatively short
777 canopy, wave reflection in the wave channel, and a simplified method used to visualise vegetation

778 motion. The canopy of 1.5 m meant that only three wave gauges could be fitted around the
 779 vegetation, which limited the number of data points that could be used to fit β_{exp} and determine its
 780 accuracy. Additionally, the reflection in the wave tank limited the number of waves that could be
 781 used for the analysis. Finally, simplifying the vegetation postures to an arc meant that postures with
 782 a double inflection point or extreme bending could not be replicated. To reduce the impact of these
 783 uncertainties, each condition was repeated three times to increase data quantity and the final model
 784 was validated against two independent data sets with real vegetation fields. Nevertheless, the
 785 limitations of our experimental approach should be considered when applying our model. We
 786 recommend that our key mechanisms and wave damping predictions will be further validated with
 787 new independent datasets across a range of wave and vegetation conditions to enhance the
 788 predictive capacity of our model.

789

790 Acknowledgements

791

792 We thank Dr. J.M. Horrillo-Caraballo, Dr. T.S. Orimoloye and Dr. A.A. Zuhaira of Swansea University,
 793 for their invaluable assistance during the laboratory experiments. Dr. Zhan Hu is thanked for
 794 providing insights on the interpretation of the CD-relation (Eq. 9). We are grateful to two anonymous
 795 reviewers whose comments have greatly improved the quality of this manuscript. TvV acknowledges
 796 support for his PhD by the College of Engineering of Swansea University. This research formed part
 797 of the Valuing Nature Programme (valuing-nature.net) which is funded by the Natural Environment
 798 Research Council, the Economic and Social Research Council, the Biotechnology and Biological
 799 Sciences Research Council, the Arts and Humanities Research Council and the Department for
 800 Environment, Food and Rural Affairs. This research was supported by the UK Research Councils
 801 under Natural Environment Research Council award NE/N013573/1, Title CoastWEB: Valuing the
 802 contribution which COASTal habitats make to human health and WellBeing, with a focus on the
 803 alleviation of natural hazards.

804

805 References

- 806 [1] M. Abdolahpour, M. Hambleton, M. Ghisalberti, The wave-driven current in coastal canopies, *J.*
 807 *Geophys. Res. Oceans.* 122 (2017) 3660–3674.
- 808 [2] M.E. Anderson, J.M. Smith, Wave Attenuation by Flexible, Idealized Salt Marsh Vegetation,
 809 *Coast. Eng.* 83 (2014) 82–92.
- 810 [3] L.N. Augustin, J.L. Irish, P. Lynett, Laboratory and Numerical Studies of Wave Damping by
 811 Emergent and Near-Emergent Wetland Vegetation, *Coast. Eng.* 56 (2009) 332–340.
- 812 [4] N. Booij, R.C. Ris, L.H. Holthuijsen, A Third-Generation Wave Model for Coastal Regions: 1.
 813 Model Description and Validation, *J Geophys Res.* 104 (1999) 7649–7666.
- 814 [5] T.J. Bouma, J. van Belzen, T. Balke, Z. Zhu, L. Airoidi, A.J. Blight, A.J. Davies, C. Galvan, S.J.
 815 Hawkins, S.P.G. Hoggart, J.L. Lara, I.J. Losada, M. Maza, B. Ondiviela, M.W. Skov, E.M. Strain,
 816 R.C. Thompson, S. Yang, B. Zanuttigh, L. Zhang, P.M.J. Herman, Identifying Knowledge Gaps
 817 Hampering Application of Intertidal Habitats in Coastal Protection: Opportunities & Steps to
 818 Take, *Coast. Eng.* 87 (2014) 147–157.
- 819 [6] K. Bradley, C. Houser, Relative velocity of seagrass blades: Implications for wave attenuation in
 820 low-energy environments, *J. Geophys. Res. Earth Surf.* 114 (2009).
- 821 [7] R.E. Britter, S.R. Hanna, Flow and Dispersion in Urban Areas, *Annu. Rev. Fluid Mech.* 35 (2003)
 822 469–496.
- 823 [8] H. Chen, Y. Ni, Y. Li, F. Liu, S. Ou, M. Su, Y. Peng, Z. Hu, W. Uijttewaal, T. Suzuki, Deriving
 824 vegetation drag coefficients in combined wave-current flows by calibration and direct
 825 measurement methods, *Adv. Water Resour.* 122 (2018) 217–227.
- 826 [9] H. Chen, Q.-P. Zou, Eulerian-Lagrangian flow-vegetation interaction model using immersed
 827 boundary method and OpenFOAM, *Adv. Water Resour.* (2019).

- 828 [10] R.A. Dalrymple, J.T. Kirby, P.A. Hwang, Wave Diffraction Due to Areas of Energy Dissipation, *J.*
829 *Waterw. Port Coast. Ocean Eng.* 110 (1984) 67–79.
- 830 [11] R.G. Dean, R.A. Dalrymple, *Water Wave Mechanics for Engineers and Scientists*, World
831 Scientific Publishing Company, Singapore, 1991.
- 832 [12] S. Fagherazzi, M.L. Kirwan, S.M. Mudd, G.R. Guntenspergen, S. Temmerman, A. D’Alpaos, J. van
833 de Koppel, J.M. Rybczyk, E. Reyes, C. Craft, J. Clough, Numerical Models of Salt Marsh
834 Evolution: Ecological, Geomorphic, and Climatic Factors, *Rev. Geophys.* 50 (2012) RG1002.
- 835 [13] J.L. Garzon, M. Maza, C.M. Ferreira, J.L. Lara, I.J. Losada, Wave Attenuation by *Spartina*
836 Saltmarshes in the Chesapeake Bay Under Storm Surge Conditions, *J. Geophys. Res. Oceans.*
837 124 (2019) 5220–5243.
- 838 [14] S.M. Henderson, Motion of buoyant, flexible aquatic vegetation under waves: Simple
839 theoretical models and parameterization of wave dissipation, *Coast. Eng.* 152 (2019) 103497.
- 840 [15] Z. Hu, T. Suzuki, T. Zitman, W. Uittewaal, M. Stive, Laboratory Study on Wave Dissipation by
841 Vegetation in Combined Current–Wave Flow, *Coast. Eng.* 88 (2014) 131–142.
- 842 [16] R.S. Jadhav, Q. Chen, J.M. Smith, Spectral distribution of wave energy dissipation by salt marsh
843 vegetation, *Coast. Eng.* 77 (2013) 99–107.
- 844 [17] G.H. Keulegan, L.H. Carpenter, Forces on cylinders and plates in an oscillating fluid, *J. Res. Natl.*
845 *Bur. Stand. Res. Pap.* 2857 (1958) 423–440.
- 846 [18] T. Koftis, P. Prinos, V. Stratigaki, Wave Damping over Artificial *Posidonia Oceanica* Meadow: A
847 Large-Scale Experimental Study, *Coast. Eng.* 73 (2013) 71–83.
- 848 [19] J.L. Lara, M. Maza, B. Ondiviela, J. Trinogga, I.J. Losada, T.J. Bouma, N. Gordejuela, Large-Scale
849 3-D Experiments of Wave and Current Interaction with Real Vegetation. Part 1: Guidelines for
850 Physical Modeling, *Coast. Eng.* 107 (2016) 70–83.
- 851 [20] B. Le Méhauté, *An Introduction to Hydrodynamics and Water Waves*, 1st ed., Springer-Verlag,
852 Berlin Heidelberg, 1976.
- 853 [21] T. Leclercq, E. de Langre, Reconfiguration of elastic blades in oscillatory flow, *J. Fluid Mech.* 838
854 (2018) 606–630.
- 855 [22] J. Lei, H. Nepf, Wave damping by flexible vegetation: Connecting individual blade dynamics to
856 the meadow scale, *Coast. Eng.* 147 (2019) 138–148.
- 857 [23] N. Leonardi, I. Carnacina, C. Donatelli, N.K. Ganju, A.J. Plater, M. Schuerch, S. Temmerman,
858 Dynamic interactions between coastal storms and salt marshes: A review, *Geomorphology.* 301
859 (2018) 92–107.
- 860 [24] I.J. Losada, M. Maza, J.L. Lara, A New Formulation for Vegetation-Induced Damping under
861 Combined Waves and Currents, *Coast. Eng.* 107 (2016) 1–13.
- 862 [25] R.J. Lowe, J.R. Koseff, S.G. Monismith, Oscillatory Flow through Submerged Canopies: 1.
863 Velocity Structure, *J. Geophys. Res. Oceans.* 110 (2005).
- 864 [26] M. Luhar, S. Coutu, E. Infantes, S. Fox, H.M. Nepf, Wave-induced Velocities inside a Model
865 Seagrass Bed, *J. Geophys. Res. Oceans.* 115 (2010).
- 866 [27] M. Luhar, E. Infantes, H. Nepf, Seagrass blade motion under waves and its impact on wave
867 decay, *J. Geophys. Res. Oceans.* 122 (2017) 3736–3752.
- 868 [28] M. Luhar, H.M. Nepf, Flow-induced Reconfiguration of Buoyant and Flexible Aquatic
869 Vegetation, *Limnol. Oceanogr.* 56 (2011) 2003–2017.
- 870 [29] M. Luhar, H.M. Nepf, Wave-Induced Dynamics of Flexible Blades, *J. Fluids Struct.* 61 (2016) 20–
871 41.
- 872 [30] M. Maza, J.L. Lara, I.J. Losada, A Coupled Model of Submerged Vegetation under Oscillatory
873 Flow Using Navier–Stokes Equations, *Coast. Eng.* 80 (2013) 16–34.
- 874 [31] M. Maza, J.L. Lara, I.J. Losada, B. Ondiviela, J. Trinogga, T.J. Bouma, Large-Scale 3-D
875 Experiments of Wave and Current Interaction with Real Vegetation. Part 2: Experimental
876 Analysis, *Coast. Eng.* 106 (2015) 73–86.
- 877 [32] F.J. Mendez, I.J. Losada, An Empirical Model to Estimate the Propagation of Random Breaking
878 and Nonbreaking Waves over Vegetation Fields, *Coast. Eng.* 51 (2004) 103–118.

- 879 [33] F.J. Méndez, I.J. Losada, M.A. Losada, Hydrodynamics induced by wind waves in a vegetation
880 field, *J. Geophys. Res. Oceans.* 104 (1999) 18383–18396.
- 881 [34] I. Möller, M. Kudella, F. Rupprecht, T. Spencer, M. Paul, B.K. van Wesenbeeck, G. Wolters, K.
882 Jensen, T.J. Bouma, M. Miranda-Lange, S. Schimmels, Wave Attenuation over Coastal Salt
883 Marshes under Storm Surge Conditions, *Nat. Geosci.* 7 (2014) 727–731.
- 884 [35] J.C. Mullarney, S.M. Henderson, Wave-Forced Motion of Submerged Single-Stem Vegetation, *J.*
885 *Geophys. Res. Oceans.* 115 (2010).
- 886 [36] J.C. Mullarney, S.M. Henderson, Flows Within Marine Vegetation Canopies, in: V. Panchang, J.
887 Kaihatu (Eds.), *Adv. Coast. Hydraul.*, World Scientific, 2018: pp. 1–46.
- 888 [37] Y. Ozeren, D.G. Wren, W. Wu, Experimental Investigation of Wave Attenuation through Model
889 and Live Vegetation, *J. Waterw. Port Coast. Ocean Eng.* 140 (2014) 04014019.
- 890 [38] M. Paul, F. Rupprecht, I. Möller, T.J. Bouma, T. Spencer, M. Kudella, G. Wolters, B.K. van
891 Wesenbeeck, K. Jensen, M. Miranda-Lange, S. Schimmels, Plant Stiffness and Biomass as
892 Drivers for Drag Forces under Extreme Wave Loading: A Flume Study on Mimics, *Coast. Eng.*
893 117 (2016) 70–78.
- 894 [39] D. Pujol, T. Serra, J. Colomer, X. Casamitjana, Flow structure in canopy models dominated by
895 progressive waves, *J. Hydrol.* 486 (2013) 281–292.
- 896 [40] K.C. Riffe, S.M. Henderson, J.C. Mullarney, Wave dissipation by flexible vegetation, *Geophys*
897 *Res. Lett.* 38 (2011) L18607.
- 898 [41] F. Rupprecht, I. Möller, M. Paul, M. Kudella, T. Spencer, B.K. van Wesenbeeck, G. Wolters, K.
899 Jensen, T.J. Bouma, M. Miranda-Lange, S. Schimmels, Vegetation-Wave Interactions in Salt
900 Marshes under Storm Surge Conditions, *Ecol. Eng.* 100 (2017) 301–315.
- 901 [42] D. Schulze, F. Rupprecht, S. Nolte, K. Jensen, Seasonal and spatial within-marsh differences of
902 biophysical plant properties: implications for wave attenuation capacity of salt marshes, *Aquat.*
903 *Sci.* 81 (2019) 65.
- 904 [43] J. Stark, Y. Plancke, S. Ides, P. Meire, S. Temmerman, Coastal Flood Protection by a Combined
905 Nature-Based and Engineering Approach: Modeling the Effects of Marsh Geometry and
906 Surrounding Dikes, *Estuar. Coast. Shelf Sci.* 175 (2016) 34–45.
- 907 [44] A. Strusińska-Correia, S. Husrin, H. Oumeraci, Tsunami damping by mangrove forest: a
908 laboratory study using parameterized trees, *Nat. Hazards Earth Syst. Sci.* 13 (2013) 483–503.
- 909 [45] A.E. Sutton-Grier, K. Wowk, H. Bamford, Future of our coasts: The potential for natural and
910 hybrid infrastructure to enhance the resilience of our coastal communities, economies and
911 ecosystems, *Environ. Sci. Policy.* 51 (2015) 137–148.
- 912 [46] S. Temmerman, P. Meire, T.J. Bouma, P.M.J. Herman, T. Ysebaert, H.J. De Vriend, Ecosystem-
913 based coastal defence in the face of global change, *Nature.* 504 (2013) 79–83.
- 914 [47] T.J. van Veelen, T.P. Fairchild, D.E. Reeve, H. Karunaratna, Experimental study on vegetation
915 flexibility as control parameter for wave damping and velocity structure, *Coast. Eng.* 157 (2020)
916 103648.
- 917 [48] V. Vuik, S.N. Jonkman, B.W. Borsje, T. Suzuki, Nature-Based Flood Protection: The Efficiency of
918 Vegetated Foreshores for Reducing Wave Loads on Coastal Dikes, *Coast. Eng.* 116 (2016) 42–
919 56.
- 920 [49] T.V. Wamsley, M.A. Cialone, J.M. Smith, B.A. Ebersole, A.S. Grzegorzewski, Influence of
921 Landscape Restoration and Degradation on Storm Surge and Waves in Southern Louisiana, *Nat.*
922 *Hazards.* 51 (2009) 207–224.
- 923 [50] R.B. Zeller, J.S. Weitzman, M.E. Abbett, F.J. Zarama, O.B. Fringer, J.R. Koseff, Improved
924 parameterization of seagrass blade dynamics and wave attenuation based on numerical and
925 laboratory experiments, *Limnol. Oceanogr.* 59 (2014) 251–266.
- 926 [51] J.T.F. Zimmerman, On the Lorentz linearization of a quadratically damped forced oscillator,
927 *Phys. Lett. A.* 89 (1982) 123–124.
- 928
929

930 **Appendix A: Description of the spatial modes**

931

932 The orthogonal spatial modes of the plant and water motion are given by

933

$$\psi_n(z_{v^*}) = (\cosh \alpha_n z_{v^*} - \cos \alpha_n z_{v^*}) + \frac{\cos \alpha_n + \cosh \alpha_n}{\sin \alpha_n + \sinh \alpha_n} (\sin \alpha_n z_{v^*} - \sinh \alpha_n z_{v^*}), \quad (\text{A.1})$$

934

935 where eigenvalues α_n satisfy

936

$$\cosh(\alpha_n) \cos(\alpha_n) - 1 = 0. \quad (\text{A.2})$$

937

938 The first three roots of Eq. A.2 are given by $\alpha_1 = 0.5969\pi$, $\alpha_2 = 1.4942\pi$, $\alpha_3 = 2.5002\pi$, and are

939 approximated by $\alpha_n = (n - 0.5)\pi$ thereafter. The spatial modes satisfy Eq. 19 and their spatial

940 derivative is given by

941

$$\frac{\partial \psi_n}{\partial z_{v^*}} = \alpha_n \psi_n. \quad (\text{A.3})$$

942

943 The four lowest order modes are shown in Fig. A.1a. The weights of the complex spatiotemporal

944 coefficients of the water motion are obtained by solving the linear system

945

$$\psi_n U_n = U_f \quad (\text{A.4})$$

946

947 where $U_f(z_{v^*})$ are the temporal coefficients of the water motion along the stem. To solve Eq. A.4,

948 the wave motion along the stem is discretised following the number of modes considered, which is

949 set at 10 in this study. A sample decomposition of a velocity profile based on linear wave theory by

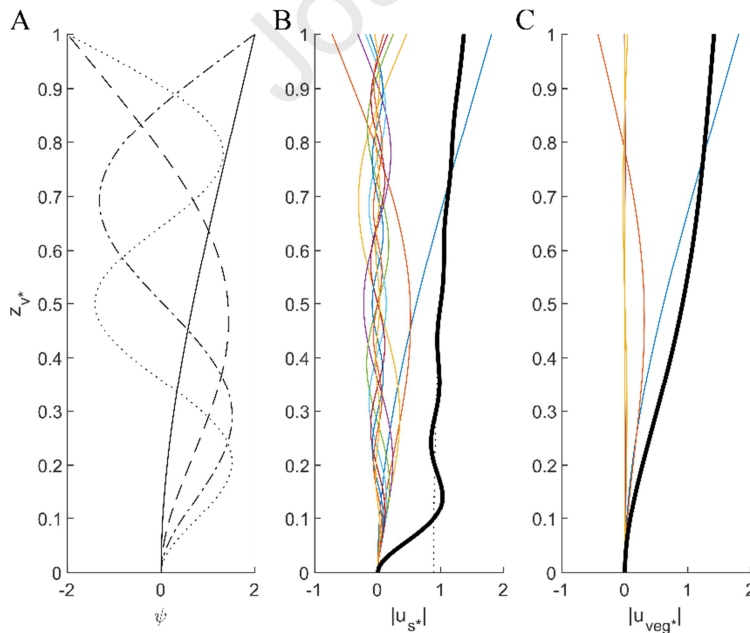
950 10 spatial modes is plotted in Fig. A.1b. Furthermore, the resulting vegetation velocity profile of an

951 artificial flexible stem under the sample forcing is shown in Fig. A.1c. While higher order modes will

952 better represent input velocity profile near the bottom, their effect on the resulting vegetation

953 velocity is negligible due to their high eigenvalues (α_n).

954



955

956 *Figure A.1: (A) The first four spatial modes ψ_n (Eq. A.1); (B) decomposition of a velocity structure given by linear wave*

957 *theory into 10 spatial modes. The thin coloured solid lines denote the weighted spatial modes, the dotted black line denotes*

958 *the input velocity profile and the thick black line denotes the sum of all spatial modes; (C) resulting vegetation velocity*

959 *structure of the artificial flexible vegetation.*

960

961 **Appendix B: Proof of a unique solution of the velocity transfer function (T)**

962

963 We substitute Eq. 21 and $Q = \frac{4}{3\pi} C_D CaL \int_0^1 (a_u - a_v) dz_{v^*}$ in Eq. 22. Furthermore, we consider the
 964 stem-averaged magnitude of both sides of Eq. 24 to obtain an expression for the stem-averaged
 965 vegetation velocity according to

966

$$\int_0^1 a_v dz_{v^*} = \int_0^1 \left| \sum \left(\frac{U_n \psi_n}{1 - \frac{4}{3\pi} C_D CaL \left(\int_0^1 a_u dz_{v^*} - \int_0^1 a_v dz_{v^*} \right)} i \alpha_n^4 \right) \right| dz_{v^*}. \quad (\text{B.1})$$

967

968

969 The stem-averaged magnitude of the vegetation velocity $\int_0^1 a_v dz_{v^*}$ is bound by $[0, \int_0^1 a_u dz_{v^*}]$. The
 970 lower bound denotes no vegetation motion and the upper bound represents full velocity transfer
 971 from water to vegetation motion. The left-hand side monotonically increases and the right-hand side
 972 monotonically decreases for increasing $\int_0^1 a_v dz_{v^*}$ within its range. Therefore, there is at most one
 973 solution of Eq. B.1.

974

975 We evaluate $\int_0^1 a_v dz_{v^*}$ at its lower and upper bound. If $\int_0^1 a_v dz_{v^*} = 0$, the left-hand side is smaller
 976 than the right-hand side of Eq. B.1. If $\int_0^1 a_v dz_{v^*} = \int_0^1 a_u dz_{v^*}$, then $Q = 0$ and the right-hand side of
 977 Eq. B.1 approaches 0. Yet $\int_0^1 a_v dz_{v^*} > 0$ at its upper bound when wave forcing is present. Thus, the
 978 left-hand side is larger than the right-hand side at the upper bound. As both sides of Eq. B.1 are
 979 continuous functions of $\int_0^1 a_v dz_{v^*}$, there is at least one solution of Eq. B.1. As we showed before
 980 that there is at most one solution, there must be exactly one solution of Eq. B.1 and Eq. 22.

Dear Professor Losada,

We would like to highlight three key results from our manuscript *Modelling wave attenuation by quasi-flexible coastal vegetation*.

- New mathematical model for simulating wave damping by coastal vegetation under quasi-flexible vegetation conditions based on the key physics in the wave-vegetation interaction.
- Wave energy dissipation over flexible vegetation is controlled by the velocity transfer from water to stem as function of wave and vegetation conditions.
- Wave damping is successfully reproduced for five vegetation species that differ in flexibility without the calibration of a drag coefficient.

Yours sincerely,

Thomas van Veelen

Declaration of interests

The authors declare that they have no known competing financial interests or personal relationships that could have appeared to influence the work reported in this paper.

The authors declare the following financial interests/personal relationships which may be considered as potential competing interests:

Journal Pre-proof